von KARMAN INSTITUTE
FOR FLUID DYNAMICS

POLITÉCNICA

Development of an efficient 3D radiation transfer solver for atmospheric entry flows

MASTER THESIS

Submitted to the Department of Aerospace and Mechanical Engineering in partial fulfillment of the requirements for the degree of Master in Aerospace Engineering at the

UNIVERSITY OF LIÈGE

and the Master Universitario en Ingeniería Aeronáutica at the

TECHNICAL UNIVERSITY OF MADRID

Author :
Javier
Martínez Martínez

Academic supervisor at ULg :
Vincent Terrapon
Academic supervisor at VKI :
Thierry Magin

Academic year 2016 - 2017

”When I first looked back at the Earth, standing on the Moon, I cried.”

Alan Shepard

Abstract

This master thesis is part of the work developed at the von Karman Institute on the assessment and calculation of the radiative conditions that influence the behavior of an spacecraft performing an entry on a planetary environment.

The evolution of research in the aerothermodynamics field has been huge over the last decades, with the development of tools to characterize the radiation field around spacecraft, and to be able to anticipate the conditions before space missions. Nevertheless, the results differ on non-negligible quantities for the different studies, due to the extreme difficulty of the correctly modelization of the radiation. The coupling of the radiative field with the flow and the ablation generated from the thermal protection systems, and the generation of new, more efficient tools are the main concerns of the ongoing research.

The main task has been to test the original code and then be capable of modifying it by introducing a multi-spectral approach, which allows to perform the calculations with a much reduced number of elements than the line-by-line traditional approach, in which the full wavelength spectrum is covered with a fine discretization, modelling the spectral contribution of individual quantum transitions. The approach has been found to reduce the computational time on more than 20 times. The results obtained showed a fast convergence of the solution with the number of bins, and a qualitatively accurate solution compared with a Monte Carlo approach. Nevertheless, the memory requirements have limited the results of this work to the use of a thousand spectral points for discretization. Accurate comparisons of the solution must require at least a hundred thousand points, and hundred bins to perform the computations.

Contents

List of acronymes

COOLFluiD	Computational Object-Oriented Libraries for Fluid Dynamics
DOM	Discrete Ordinates Method
FV	Finite Volume
HSNB	Hybrid Statistical Narrow Band
LBL	Line-By-Line
LTE	Local Thermodynamic Equilibrium
MC	Monte Carlo
MPI	Message Passage Interface
Mutation++	Multicomponent Thermodynamic And Transport properties for Ionized gases in C++
RANS	Reynolds-averaged Navier-Stokes
RTE	Radiative Transfer Equation
SNB	Statistical Narrow Band
ZM	Zonal Method

List of symbols

η = Emission coefficient [W/m^3/sr/m]

κ = Absorption coefficient [1/m]

σ = Wavelength [m]

τ = Optical depth []

c = Speed of light [m/s]

h = Planck constant [J s]

k = Boltzmann constant [J / K]

I_σ = Spectral intensity [W/sr/m^2]

ib = Bin index

p = Pressure [Pa]

S = Source radiative term [W/m^2] - Surface of the element [m^2]

T = Temperature [K]

Å = Angstrom

V = Volume [m^3]

Acknowledgments

Dedicado a todos aquellos que me han ayudado a llegar hasta aquí. Especialmente a mi familia, que ha estado ahí siempre, y para la que todo lo que pueda decir aquí se queda corto. Son ellos los que han estado a mi alrededor durante todos los años en los que paso a paso he podido convertirme en lo que soy ahora.

On the professional aspect, I would like to thank, first of all, to Thierry Magin, for having given me the opportunity to perform the master thesis at the von Karman Institute. His work leading the team makes possible extremely valuable investigation, in an environment in which team work is a very positive experience. Thank you as well, for all the time dedicated to the small things that were very valuable for me.

Thank you as well to Andrea Lani, not only for all the work he has done on the improvement of the code, and for the amazing work performed with the COOLFluiD environment (which has been fundamental for the development of this work), but also for integrating me on the group and for giving me useful advices when I was completely lost.

I would like to thank as well Alejandro Álvarez Laguna and James B. Scoggins. To Alejandro, for being the first person that helped me when I arrived at VKI. His kind explanations of the base code, and of everything I needed were of great help to make the first contact with the work. To JB, for his help also when it was needed, and his explanations on the radiation computations.

I would like to thank as well Vincent Terrapon, professor at the Université de Liège, for accepting to become my university mentor in this task.

And last, but not least, I want to thank the rest of people at VKI, and especially the stagiares that have been here over these months. Claudio, who has been part as well of the radiation group, and suffered with me, Guille, Corra, Carmelo, Dario, Riccardo, Aurélien, Piero, Domenico... I could not have had a better environment to perform the work (and the not-work).

Introduction

Of all the technological developments that humans have carried out over the last decades, space exploration is probably the most exciting and challenging. The extreme conditions that the spacecraft suffers from its launch to its end-of-life, and the restrictions imposed by both external and internal constraints during the whole mission make it a complex problem to analyse.

This complex analysis can be then subdivided into different parts, which are coupled between them. Each subsystem on the spacecraft must be capable of accomplishing its requirements to make the mission successful. Of all these requirements, the protection of the spacecraft against the atmospheric reentry conditions constitutes one of the main challenges that a spacecraft faces when it tries to reach its objective. An enormous amount of heat, combined with a a chemically reactive environment make of it one of the main concerns for engineers when a planetary mission, manned or not, is to be planned.

Radiative processes play a significant role in most of the problems related to atmospheric physics, astrophysics and spacecraft analysis. The spectral and spatial variation of the radiative properties make the estimation of the radiative fluxes over a spacecraft extremely difficult to calculate. The main objective of this project has been the implementation of approaches to analyse the problem of re-entry radiation in 3D configurations, and to be able to compute the radiative fluxes around them in an efficient manner.

Several successful attempts to create an efficient radiation solver code can be found in literature. Especially interesting is the work of the aerothermodynamics group at NASA, with the creation of the NEQAIR database for radiative computations, and the development of accurate tools to reproduce the re-entry conditions [Wray 2012], [Johnston 2008]. In Europe, the main research activities on radiation in reentries are being performed at ESA, which is funding several lines of research, DLR, with the development of the TAU code and its validation, and VKI, whose main research topics in the aerothermodynamics area are outlined in section 1. Although most of the investigation that is being carried out in the re-entry field is based on methods that provide a very precise solution for the radiative problem, like the Monte Carlo method with a Line-By-Line approach to compute the radiative coefficients, more and more research is starting to be developed in order to approximate the solution with much less computationally expensive codes.

In order to be able to create an efficient solver to calculate the heat fluxes on a wide range of configurations and atmospheric components, the first part of the thesis has been dedicated to the understanding of the physical model behind radiation, and its computational approach. The original Finite Volume code developed at NASA Ames in collaboration with VKI, and which allowed the computation of the radiative fluxes for an Earth reentry, has been validated for some simple configurations.

The second part of it is dedicated to the work performed on the development of a multi-spectral approach to reduce the computational time, maintaining a high level of accuracy. Chapter 3 is dedicated to perform an exhaustive analysis on the influence that the different parameters have on the spectral distribution. This is a mandatory step in order to correctly perform the calculations on chapter 4, in which this approach is then applied for the calculation of the radiative flux divergence on a real model, the FireII spacecraft, developed by NASA.

The last part of the report is dedicated to further analyse the problem, give a brief overview of the future work that has already been started at VKI, and to provide the conclusions extracted from this work.

Chapter 1

Radiative transfer on re-entry configurations

1.1 The radiative transfer problem

In the beginning of the space exploration era, the lack of understanding of the re-entry physical phenomena, and of tools to correctly estimate the heat fluxes on the spacecraft return to Earth, leaded to designs that over-estimated the thickness of the thermal protection systems on the spacecraft. This tendency, however, has drastically changed, as the funding of space exploration programs decreases over time, making necessary an estimation of the heat load around the spacecraft as accurate as possible to minimize the necessary weight of the mission.

The re-entry problem can be defined as follows. The spacecraft arrives to its target with a very high speed (10 km/s typically on an Earth reentry), which generates a shock layer in front of the probe. This shock layer is responsible for a huge increase in the temperature and pressure on the area between the shock and the spacecraft. With these pressure and temperature conditions existent, the gas becomes ionized, and a plasma is formed. This plasma will emit radiation, which increases the heat load on the spacecraft and which will couple with the flow. The difficulty of the problem lies then on the strong coupling of these fields. As the plasma is a strongly participating medium, because it can both emit and absorb the radiation, it makes the problem extremely complicated to be solved.

The problem is even more difficult to predict if we consider that, in most modern spacecrafts, the approach to reduce the heat load arriving to the spacecraft is to use an ablative material as a protecting coat. This material is chemically degraded with the heat, releasing chemical species which couple with the radiative field and the flow. This three dimensional fully coupled problem is the objective to study to anticipate the conditions for

a new mission.

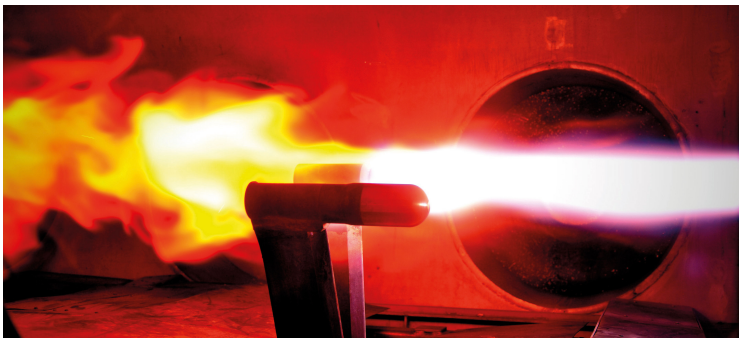

Figure 1.1: Ablation test in the Plasmatron facility

Over this work, the analysis will be restricted to the problem of the radiative transfer prediction, and we will do it in an uncoupled way; this is, by using the solution of the flow around the spacecraft to compute the radiative properties, without giving a feedback to the flow. This approach is only a previous step on the coupling between the flow and the radiative field, because to achieve the real conditions, an iteration is needed between them.

1.1.1 Physical description of the problem

Radiative transfer is the phenomenon produced by the transfer of energy in the form of electromagnetic transitions. The photons, or waves, travel through a medium producing radiative exchanges of energy which fall into the atomic level. The photons travel at the light speed in vacuum, and at a lower speed in mediums with an index of refraction higher than one:

$$c_{ph,i} = \frac{c_{ph,v}}{n} \tag{1.1}$$

where $c_{ph,i}$ represents the speed of the photon in the medium i, $c_{ph,v}$ represents the speed in vacuum, and n is the index of refraction. The energy carried by a photon with a certain electromagnetic wavelength is related with this speed by the Planck-Einstein relation as:

$$E = \frac{hc}{\sigma} = hf \tag{1.2}$$

where h is the Planck constant, and the frequency f and the wavelength σ are related by the speed c. The electromagnetic spectrum is the discretization into regions of all these wavelengths or frequencies:

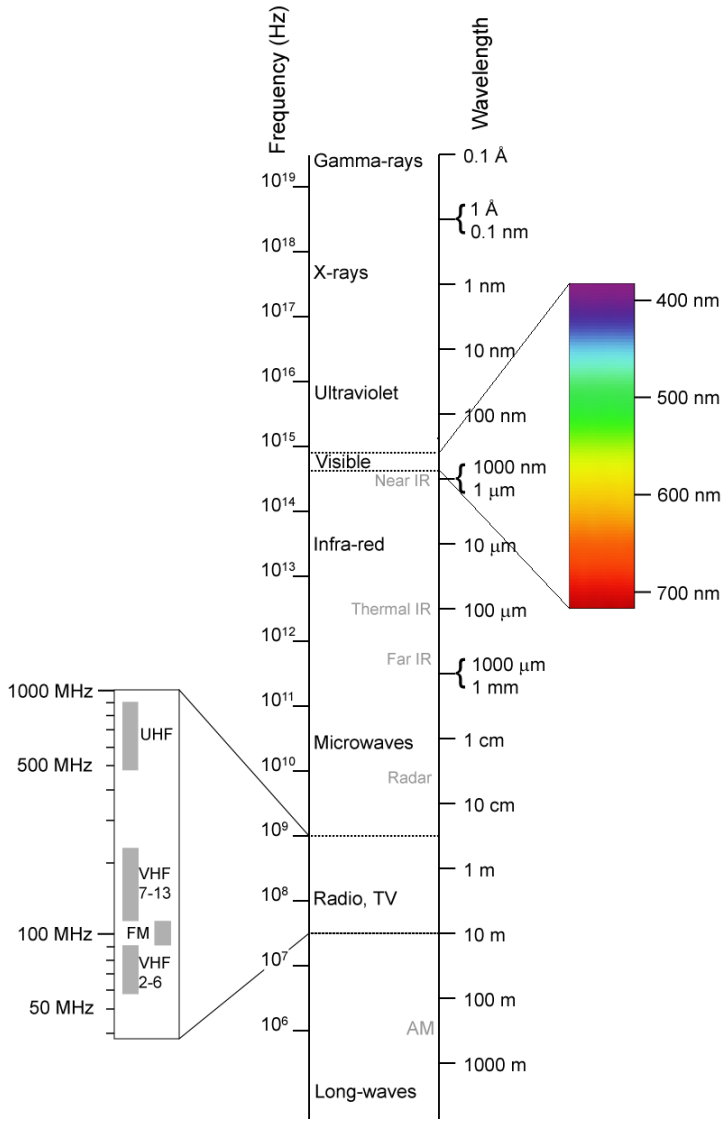

Figure 1.2: Electromagnetic spectrum [Victor Blacus]

Of all these regions, the region of interest for aerothermodynamics is mainly the thermal radiation, which ranges from the ultraviolet region to the infrared one. To provide an example, the range of wavelengths measured by the calorimeters on the FireII spacecraft went from 0.2 to 4 µm [Wright 2003].

The equation that drives the behavior of the radiation field is the Radiative Transfer Equation (RTE). The equation, described below, is a differential equation lagrangian in nature, and it describes the variation of the radiative spectral intensity with respect to the radiative coefficients, this is, the elemental processes that define radiation on a media -absorption, emission and scattering-. On its most elemental form, following [Modest 2013]

or [Vincenti 1986], the RTE takes the form stated in (1.3):

$$\frac{1}{c}\frac{\partial}{\partial t}I_\sigma + \vec{\Omega}\cdot\nabla I_\sigma + (\kappa_{\sigma,s}+\kappa_{\sigma,a})I_\sigma = \eta_\sigma + \frac{1}{4\pi}\kappa_{\sigma,s}\int_\Omega I_\sigma d\Omega \tag{1.3}$$

where I_σ is the radiative spectral intensity, $\vec{\Omega}$ is the direction of propagation, η_σ is the emission coefficient, $\kappa_{\sigma,s}$ is the scattering opacity and $\kappa_{\sigma,a}$ is the absorption opacity. The resolution of the equation is non-trivial, and no analytical solution can be found but in very specific and simplified configurations. The scattering on equation (1.3) can be neglected in gaseous media without solid particles, as the scattering coefficient, computed by using equation (1.4) is very low.

$$\kappa_s = \frac{p\sigma_s}{kT} \tag{1.4}$$

where k is the Boltzmann constant, p is the pressure, T the temperature and σ_s the Raileigh scattering cross section. This coefficient, which represents the inverse of the mean free path of a photon before the scattering is produced, is of the order of $10^{-6}m^{-1}$ on an usual reentry configuration (10000 K, $10^5 Pa$, $\sigma_s = 10^{-30}m^2$) [Karl 2013]. This can be then neglected on a preliminary study compared with the absorption coefficients for air at the same conditions, which are from 10 to 1000 times larger.

Neglecting scattering and the unsteady effects, as the medium can be supposed stationary with respect to the speed of light, equation 1.3 can then be written as:

$$\vec{\Omega}\cdot\nabla I_\sigma + \kappa_{\sigma,a}I_\sigma = \eta_\sigma \tag{1.5}$$

This form of the equation is much more simpler to solve as the light travels in a straight line, since the scattering effects have been neglected. A general solution for this equation can be then found in terms of the absorption and emission coefficient.

$$I_\sigma(s) = I_\sigma(s_0)e^{-\tau_\sigma(s_0,s)} + \int_{s_0}^{s}\eta_\sigma(s')e^{-\tau_\sigma(s',s)}ds' \tag{1.6}$$

where s_0 and s represent two positions in the problem, and τ_σ is the optical depth of the medium, this is, the logarithmic adimensional quantity which represents the ratio of the incident to transmitted radiant power through a medium, and which can be expressed as a function of the already stated variables as:

$$\tau_\sigma(s_0,s) = \int_{s_0}^{s}\kappa_\sigma(s)ds \tag{1.7}$$

The two position points s_0 and s to compute (1.6) can be chosen as desired over the problem, but an easy solution is to choose the points at the boundary of the problem as the

zero points, and then compute the equation from this point to the end of the domain.

Although the problem has been simplified from its original configuration, the RTE equation is still extremely challenging to solve because of the non-local effects and its spectral features. Reentry flows are extremely participating mediums, in which absorption and emission change drastically from one zone to another. Figure 1.3 shows an spacecraft configuration in which a shock is formed in the front part of the body, and creates a thermo-chemical non-equilibrium zone in which the radiative properties are rapidly changing. This shock excites the translational and rotational modes and generates a heating environment in which the internal nodes of vibration are lagging behind the other two. This can be seen by looking at the shape of the temperatures on the figure, in which T_v represents the vibrational temperature and T, the translational one.

After this first shock layer region, a thermal equilibrium region appears for many configurations. This region, in which chemical non equilibrium is still present, generates most of the radiation in the problem, which comes mostly from the atomic line radiation. This phenomenon can be seen on the spectral features in this region in the figure, where the presence of the atomic lines for nitrogen and oxygen clearly dominates the radiation distribution. Finally, the boundary layer region, the closest region to the body, is characterized by a cooling, which is associated to a two temperature model, in which the vibrational temperature can be hotter than the translational one. This region is mainly dominated by absorption, as opposite to the other regions, in which emission was predominant.

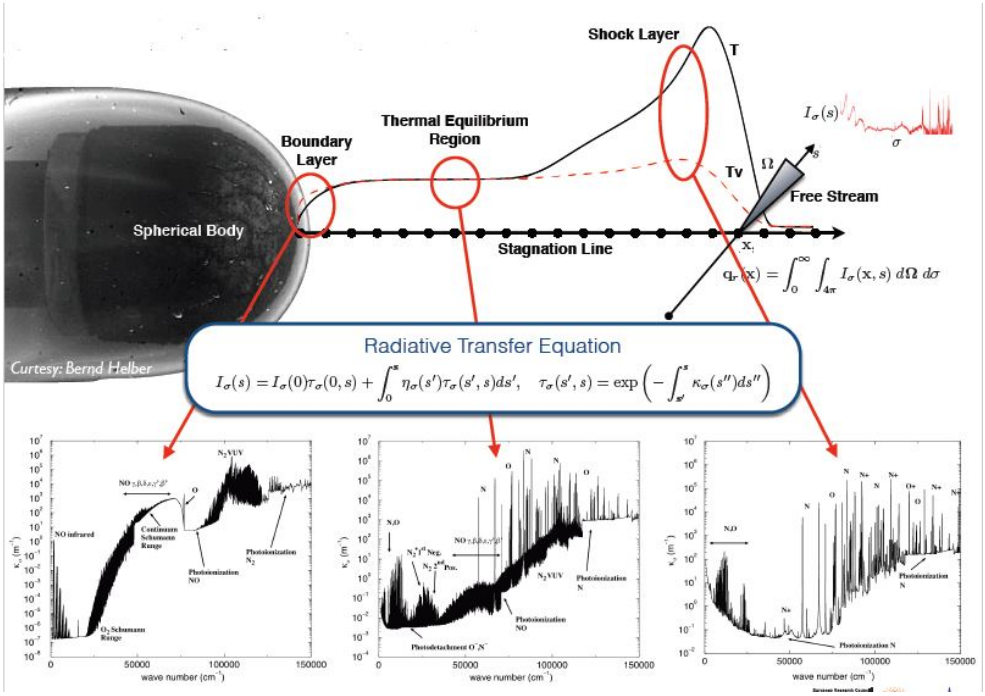

Figure 1.3: Radiative zones behind a reentry configuration probe [Scoggins]

1.2 Numerical and experimental methods to approach the reentry problem

Effort has been put over the last section to emphasize that the reentry problem is extremely complicated to solve, both in terms of physical understanding and modelling and in computational cost. There are few groups of investigation dedicated to research this problem, and most of them interconnected to share data to improve the results of future projects on the field.

At VKI research is being performed both with numerical and experimental methods. The main tools used at the Institute to characterize reentries are resumed in the following table:

Facilities at vKI	
Numerical	COOLFluiD Mutation++
Experimental	Plasmatron Longshot

The analysis of the experimental tools is out of the interest for this report, and the interested reader can refer to [Bottin 2000] and [Richards] for further information on the

Plasmatron and Longshot facilities respectively.

1.2.1 Mutation++

Mutation ++ is a computational library which allows the computation of the flow thermodynamic and transport properties. It allows to compute and perform, among other tasks:

- Thermodynamic properties
- Multicomponent transport properties
- Finite rate chemistry in thermal nonequilibrium
- Robust multiphase equilibrium solvers

Although the library is mostly used to compute the properties in problems where the flowfield solution is coupled with the radiative field, it has been used on this scope to compute the flow on the Monte Carlo solution for comparison with the code, and as a way of checking the species present in the flowfield. Further information on the library development can be found in [Scoggins 2014] .

1.2.2 COOLFluiD

COOLFluiD is a component-based framework for scientific high-performance computing, CFD and multi-physics applications. It was originally developed at the Von Karman Institute for Fluid Dynamics based on the work of Lani and Quintino [Lani 2013]. The framework allows to perform multi-physics simulations with a wide range of spatial discretization algorithms and time marching methods, both explicit and implicit. It has allowed us to perform coupled, parallel simulations on hypersonic flows, with highly flexible implementation and configuration capabilities. Apart from these, some other features of the software are:

- Multiple Physical Models: Hypersonic flows in LTE and non-LTE configurations, Heat Transfer problems, Linear Elasticity, Turbulence RANS Models, Incompressible Flows
- Parallel Computations: MPI, CUDA support
- Space Discretizations: Cell Centered Finite Volume, Residual Distribution Finite Element, Spectral Finite Volume, Spectral Finite Difference, Discontinuous Galerkin

- Time Integration Schemes: Runge Kutta, 1 and 3 point Backward Euler, Crank-Nicholson, Time Limited Schemes
- Coupled Systems Simulations: Aeroelasticity, Aerothermoelasticity, Heat Transfer coupled problems

The COOLFluiD platform has been the main tool in which the code necessary for the development of this thesis has been created. Most the code generated for this work has been created by using the C++ programming language.

Chapter 2

Resolution of the Radiative Transfer Equation

2.1 Methods to solve the RTE

The resolution of the RT equation is non-trivial, and analytical or semi-analytical solutions can be obtained only when the geometry and boundary conditions of the problem are very simple and well known. If this conditions are not fulfilled, as happens in most of real configurations, two main methods are considered to solve the equation numerically; the Monte Carlo ray tracing methods, and the Finite Volume methods. There are few other methods, like the Zonal Method [Caliot 2010], but we will restrict ourselves in this scope to the two previously mentioned ones.

2.1.1 Finite Volume solver for radiative computations

In this section, the mathematical equations on which the algorithm is based will be explained, with an emphasis on the physical meaning of each of the parameters.

The 1-D RTE equation for a non-scattering plasma in the direction Ω is expressed as:

$$\vec{\Omega} \cdot \vec{\nabla} I_\sigma(\Omega) = \kappa_\sigma S_\sigma - \kappa_\sigma I_\sigma \tag{2.1}$$

where S_σ is the source term, equal to the ratio between the emission and the absorption coefficient, and which in LTE conditions equals the black body spectral intensity. This equation can be then integrated over the computational domain V.

$$\int_V \vec{\Omega} \cdot \vec{\nabla} I_\sigma dV = \int_V \vec{\nabla} \cdot (\vec{\Omega} I_\sigma) dV = \int_S I_\sigma \vec{\Omega} \cdot d\vec{S} = \int_V \kappa_\sigma (S_\sigma - I_\sigma) dV \tag{2.2}$$

We can now perform the discretization to be able to solve the problem in our computational domain by approximating the volume integrals with the value of the integrand at the

center of the computational element times the volume, while the surface integral can be discretized with a summation over the faces of the values in the center of the faces, with index k, multiplied by the corresponding areas.

$$\sum_k I_{\sigma,c}(\Omega)\vec{\Omega}\cdot\triangle\vec{S_k} = \kappa_{\sigma,c}(S_{\sigma,c} - I_{\sigma,c}(\Omega))V_c \tag{2.3}$$

Next step will be to split the surface summation into the incoming and the outgoing parts of the radiative intensity, as it is stated in equation (2.4)

$$\sum_{kI_\sigma\vec{\Omega}\cdot\triangle\vec{S_k}<0} I_{\sigma,k}(\Omega)\cdot\triangle\vec{S_k} + \sum_{kI_\sigma\vec{\Omega}\cdot\triangle\vec{S_k}>0} I_{\sigma,c}(\Omega)\vec{\Omega}\cdot\triangle\vec{S_k} = \kappa_{\sigma,c}(S_{\sigma,c} - I_{\sigma,c}(\Omega))V_c \tag{2.4}$$

where $\vec{S_k}$ is the outward-pointing surface area vector of face k of the cell.

If we solve this equation we come with the final form of the intensity equation for the given direction:

$$I_{\sigma,c}(\Omega) = \frac{-\sum_{kI_\sigma\vec{\Omega}\cdot\triangle\vec{S_k}<0} I_{\sigma,k}(\Omega)\vec{\Omega}\cdot\triangle\vec{S_k} + \kappa_{\sigma,c}S_{s,c}V_c}{\sum_{kI_\sigma\vec{\Omega}\cdot\triangle\vec{S_k}>0}\vec{\Omega}\cdot\triangle\vec{S_k} + \kappa_{\sigma,c}V_c} \tag{2.5}$$

But this approach fails when facing problems in which the source term is varying quickly, or when the opacity term is large, as happens in optically thick media [Wray 2012]. There is another approach proposed in the mentioned article that we can follow in order to solve the problem. Starting again with the general form of the equation, (2.6)

$$\vec{\Omega}\cdot\nabla I_\sigma + \kappa_\sigma I_\sigma = \kappa_\sigma S_\sigma \tag{2.6}$$

We now introduce an exponential factor, reformulating the solution of the RTE expression as:

$$\overline{I}(s,\Omega) = \overline{I}(0,\Omega)e^{-\kappa s} + (1 - e^{-\kappa s})S \tag{2.7}$$

which is the 1-d exact RTE solution for constant opacity and radiative source term along a direction Ω, and where $\overline{I}(s,\Omega)$ is the cross-sectional average intensity at distance s in this direction.

The average incoming intensity $\overline{I}(0,\Omega)$ in equation 2.7 can be computed as the average intensity over all faces which have an incoming radiation for the considered direction. If

we solve the equation to get the intensity for the outgoing faces:

$$I_{\sigma,ko}(\Omega) = \frac{\sum_{i,\vec{\Omega}\cdot\triangle\vec{S}_i<0} \overline{I_{\sigma,ki}}(\Omega)|\vec{\Omega}\cdot\triangle\vec{S}_i|}{\sum_{i,\vec{\Omega}\cdot\triangle\vec{S}_i<0}|\Omega\cdot\triangle\vec{S}_i|} e^{-\kappa_c d} + (1-e^{-\kappa_c d}) \tag{2.8}$$

where *ko* and *ki* represent the outgoing and ingoing faces respectively. If the source term is then approximated for direction $\vec{\Omega}$ as a function of the effective cross-cell propagation distance d for that direction:

$$S_\sigma(x) \simeq \begin{cases} S_{\sigma,ki} + (S_{\sigma,c} - S_{\sigma,ki})\frac{x}{(d/2)} & \text{if } 0 \le x \le \frac{d}{2} \\ S_{\sigma,c} + (S_{\sigma,ko} - S_{\sigma,c})\frac{x-(d/2)}{(d/2)} & \text{if } \frac{d}{2} \le x \le d \end{cases} \tag{2.9}$$

A solution for the incoming and outcoming values of the radiative source term can be obtained, by doing an average of the central value S_c and the average-weighted averages of the neighboring central values.

$$S_{\sigma,ki} = \frac{1}{2}(S_{\sigma,c} + \frac{\sum_{i,\vec{\Omega}\cdot\triangle\vec{S}_i<0} S_{\sigma,ki}(\Omega)|\vec{\Omega}\cdot\triangle\vec{S}_i|}{\sum_{i,\vec{\Omega}\cdot\triangle\vec{S}_i<0}|\vec{\Omega}\cdot\triangle\vec{S}_i|}) \tag{2.10}$$

$$S_{\sigma,ko} = \frac{1}{2}(S_{\sigma,c} + \frac{\sum_{i,\vec{\Omega}\cdot\triangle\vec{S}_i>0} S_{\sigma,ki}(\Omega)|\vec{\Omega}\cdot\triangle\vec{S}_i|}{\sum_{i,\vec{\Omega}\cdot\triangle\vec{S}_i>0}|\vec{\Omega}\cdot\triangle\vec{S}_i|}) \tag{2.11}$$

This solution can be finally solved to come with the solution for the radiative intensity at the center of the cells, equation 2.12.

$$I_{\sigma,c}(\Omega) = \frac{\sum_{i,\vec{\Omega}\cdot\triangle\vec{S}_i<0} \overline{I_{\sigma,ki}}(\Omega)|\vec{\Omega}\cdot\triangle\vec{S}_i|}{\sum_{i,\vec{\Omega}\cdot\triangle\vec{S}_i<0}|\vec{\Omega}\cdot\triangle\vec{S}_i|} e^{-\frac{1}{2}\kappa_c d} + (1 - \frac{1-e^{-\frac{1}{2}\kappa_c d}}{\frac{1}{2}\kappa_c d})S_{\sigma,c} + (\frac{1-e^{-\frac{1}{2}\kappa_c d}}{\frac{1}{2}\kappa_c d} - e^{-\frac{1}{2}\kappa_c d})S_{\sigma,ki} \tag{2.12}$$

2.1.2 Monte Carlo methods for radiative computations

Although this work has been dedicated to the study of an FV solver to compute the radiative fluxes, the method does not offer the best accuracy on the solution. The state-of-the-art method in radiative transfer solving is the use a Monte Carlo method.

The Monte Carlo approach is an statistical, random-based approach which approximates the problem by dividing the energy of the medium into an integer number of particles, whose properties, like wavelength, direction or position are randomly assigned, pondering

this choice with their relevance.

The main advantage of the Monte Carlo methods is that can we can reach a very accurate solution with a highly enough number of photons. The main disadvantage is that, the increase of this number of photons increases the computational time of the simulations. In the end, Monte Carlo methods offer a highly accurate solution which can be used in detailed design phases, whereas the rest of the methods, especially the FV one, are a better option for preliminary design phases.

2.2 Finite Volume benchmark code

In this subsection, the source code will be explained and commented. This chapter is fundamental and serves as a base to develop the concepts which will make part of the thesis. This explanation is based in the technical notes developed at NASA Ames by Alejandro Álvarez Laguna, Nagi Mansour and Jeremie Meurisse, as part of the work developed there, and in the validation phase that has been developed over the first months of the work at the von Karman Institute.

The structure of the base code can be divided into 4 main parts:

1. Mesh reading. In order to perform the computation of the radiative fluxes, a CFD mesh has to be provided to the solver. This mesh can be structured or unstructured, which makes possible the treatment of problems with highly asymmetric configurations. In this step, the geometrical entities of the studied configuration are computed and stored:

    - Number of cells
    - Cell ID
    - Coordinates of the cell centers
    - Coordinates of the cell nodes

2. Directions computation. The first real step of the algorithm is the computation of directions. In this phase, the user must select the number of directions desired (8,24,48 and 80 directions were implemented in the base code), and then the directions are computed based on a DOM method. More information about this method can be found in [Modest 2013] and in the appendix 1. Basically, this method is based on numerical quadratures which replace the integrals over the directions needed to solve the problem. These directions are defined by the weight associated to the quadrature

and by the direction $\vec{s}$, which is represented by the direction cosines with respect to the principal directions:

$$\vec{s} = (\vec{s} \cdot \vec{i})\vec{i} + (\vec{s} \cdot \vec{j})\vec{j} + (\vec{s} \cdot \vec{k})\vec{k} = \xi\vec{i} + \eta\vec{j} + \mu\vec{k} \tag{2.13}$$

As a remark, complex configurations may need many more directions than 80 to be able to offer a smooth solution of the problem. To this extent, parallel work to the author's has been done in order to be able to handle any arbitrary number of directions, based on an algorithm developed by Dr. Alessandro Munafò [1].

3. Advance order. Once the directions are physically established, the algorithm needs to know which cells of the mesh are on each of the directions. To do so, the advance order algorithm, for each of the directions, sweeps over all the computational cells, and over all the faces, as follows:

   - Sweep over all the cells
   - Sweep over all the faces of the cell. If the dot product of the direction d and the normal to the face is negative then check that the neighbor is already swept. If both conditions are true, the algorithm returns to the cell loop.

4. Computation of the opacities. This has been the main focus of the present work, as it was the main weakness of the original code. In the source code, the opacities were computed from two tables. These tables provided values for the absorption coefficient and the source term for two pressures (1 and 10 atmospheres) and several temperature values (from 300 K to 15000 K), for an air mixture. The tables divided the spectrum into a hundred bins, so the values provided were the average values of the spectral properties for the T and p conditions selected. As this only offers a set of discrete values, the values for the real configuration computed were interpolated from the current T, p and ib.

5. Computation of the radiative fluxes. Once the values for the absorption and source term have been computed, we can use (2.5) or (2.12) in order to compute the radiative intensity, for a given bin and direction. From this intensity, the radiative flux and its divergence can be computed as follows:

$$\vec{q}^{rad} = \sum_{x=1}^{N_b} \sum_{y=1}^{N_d} \sum_{z=1}^{N_e} a_d I^d_{\sigma,e} \vec{\Omega}_d \tag{2.14}$$

$$\nabla \cdot \vec{q}^{rad} = \sum_{x=1}^{N_b} \sum_{y=1}^{N_d} \sum_{z=1}^{N_e} \frac{a_d I^d_{\sigma,e} \vec{\Omega}_d \cdot \triangle \vec{S}_e}{V_e} \tag{2.15}$$

[1] University of Illinois, Urbana-Champaign

These equations are further explained in chapter 4.

2.3 Spherical case

The first part of the work to make this thesis possible has been dedicated to understand how the base code worked, to validate it, and to perform a parametric study to be able to determine the influence of the different parameters on the final results, and on the accuracy of the solutions obtained. The testcase used from now on will be a sphere of 1.5 cm of radius, on a constant pressure field, and with a Gaussian temperature profile, as it will be further explained later.

On this path, the first step of the study will be dedicated to analyse the number of radial points chosen for the integration of the fluxes over the radius, because this value will be then fixed for the rest of the validation simulations. Two meshes for the analysis, a 22 x 22 x 22 points mesh, and a thinner one with 100 points in the radial direction have been studied. To perform an integration over all the angles in order to determine the heat fluxes and their divergence, as the mesh is unstructured, an average is done between all the points which are between each pair of radius. As the number of radial points that we choose can be much greater than the number of points of the mesh in the radial direction, it can happen that we arrive to a situation in which we get 0 points to do the average between two of the radial points. This will lead to peaks in the radial data solution if the number of points is not chosen carefully. On the other hand, we should select a high number of points to reproduce a correct solution.

So, the first analysis in this parametric study is going to be the minimum number of radial points who guarantees smoothness in the solution, being the maximum possible to guarantees accuracy on the results. Starting on 100 points on the coarser mesh the number of points was first increased to 200, showing a huge number of peaks on the solution. This number of points has been then decreased to 100, 30, 25 and 21 points. The results for the one hundred and 21 points cases are shown below:

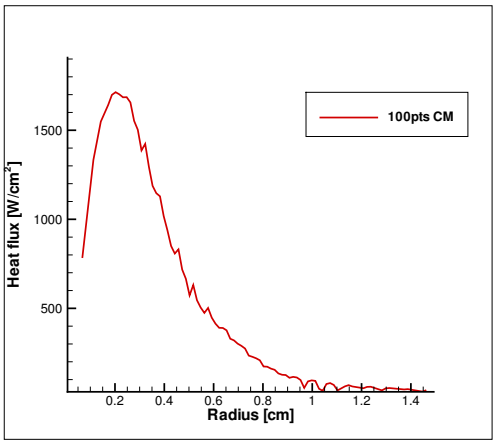

(a) 100 radial points integration

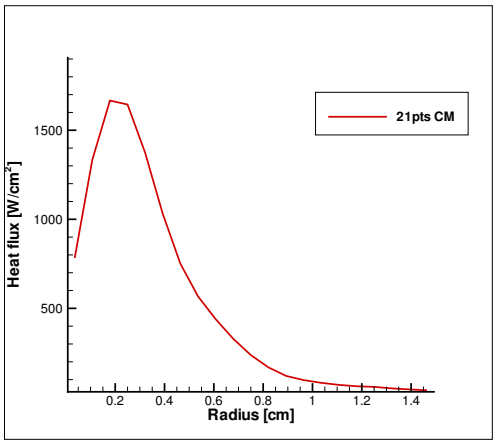

(b) 21 radial points integration

Figure 2.1: Radial flux data as a function of radial points for the coarser mesh

from which it can be clearly extracted that using a high number of points on this mesh leads to discontinuities on the solution, whereas using few points may lead to great differences on the solution, as it will be shown in section 2.5.

This situation improves when we use a thinner mesh, where the number of points over which we compute the flux increases, and therefore we can increase the number of radial points without loosing the physical meaning of the problem. The same comparison than before is then presented below:

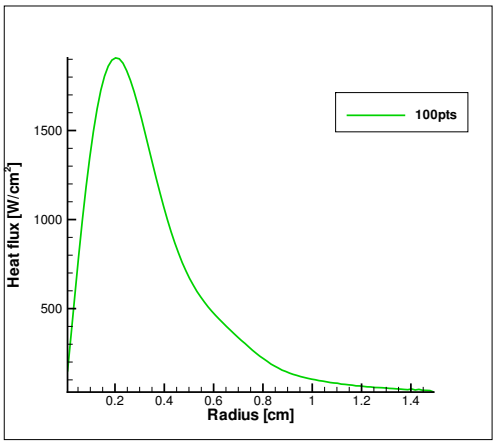

(a) 100 radial points integration

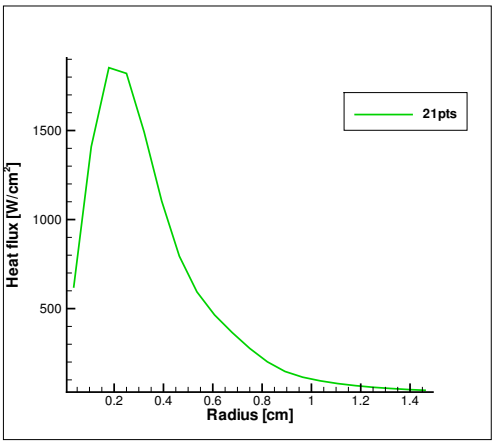

(b) 21 radial points integration

Figure 2.2: Radial flux data as a function of radial points

Figure 2.2 shows the results for the thinner mesh. Comparing these results with figure 2.1, it is clear that the solution is smoother for a given number of radial points, and this situation is even more dramatically increased for the case of the highest number of points shown

in the analysis, this is, a hundred points. Moreover, the use of a thinner mesh increments the heat flux peak on around 150 W/m^2, which is closer to the analytical solution as will be demonstrated later.

For most of the analysis that follow we will restrict ourselves to the case of the most accurate mesh, although it is interesting in some cases to check as well the comparison between the two meshes. For figures 2.1 and 2.2, and from now on in section 2.3, the units for the parameters inside the code, and the results are the ones described in 2.1.

	Units
I_ν	$[W/cm^{-2}]$
κ_ν	$[cm^{-1}]$
S_ν	$[W/cm{-}2]$
$\vec{q}$	$[W/cm^{-2}]$
$\nabla \cdot \vec{q}$	$[W/cm^{-3}]$

Table 2.1: Units for the different parameters

This poses a new question. The number of points have been selected to find a balance between the accuracy of the solution and the smoothness of it. Few points guarantee a smooth solution on the outer layer of the sphere, but can lead to poorer results in the central part, where greater gradients of temperature and radiative fluxes exist. This leads to the following question: Is it possible to use a greater number of points, 100 points as an example for the thinner mesh, without loosing precision on the outer part?

To address this phenomenon, the physical interpretation of this must be done. This happens because in this outer zone, few points of integration exist between bins, and therefore, we loose continuity on the solution. On the next graphs, a comparison between two cases with 48 directions on the thinner mesh are performed.

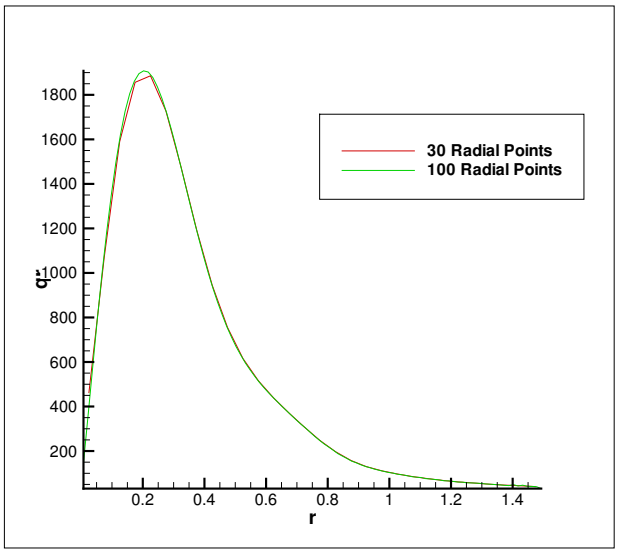

Figure 2.3: Comparison of radial data flux for 100 and 30 radial data points

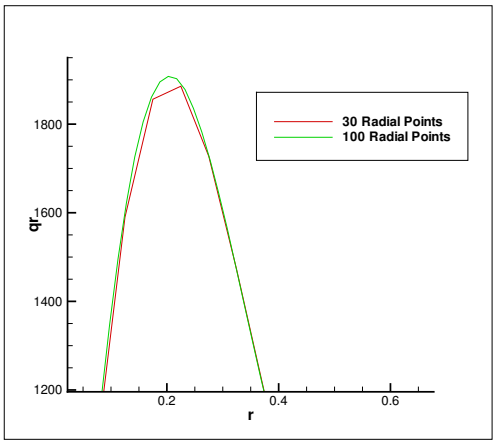

(a) Detail on the central part of the sphere

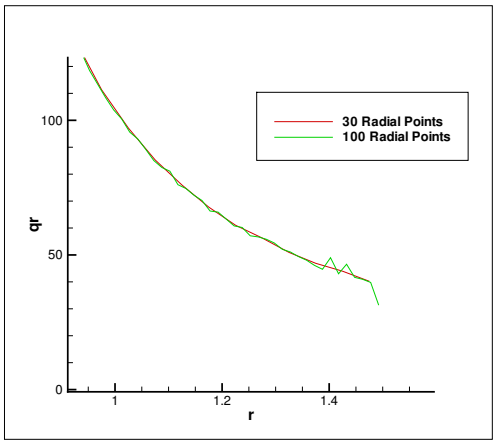

(b) Detail on the outer part of the sphere

30 points have been selected based on this results for the case of the first mesh, and 100 for the case of the thinner mesh. This is because greater accuracy on the results is needed in the inner part of the sphere, where the gradients are bigger than in the outer part, in which nevertheless resolution is lost because the mesh is more spaced. With this approach, the solution is expected remain closer to the true values of the radiative fluxes, hypothesis which has to be proven over the following steps of the work.

Next thing that has been done is to make a study on the accuracy of the solution as a function of the number of directions that is considered. The choices of directions are restricted for the moment to 8, 24, 48 and 80, for which exact quadrature values are provided. This is not a fix number and could be increased in the future if needed. As

an easy way to see the influence with the directions, the fluxes over the sphere can be visualized. This is what is shown in figures 2.5 to 2.7.

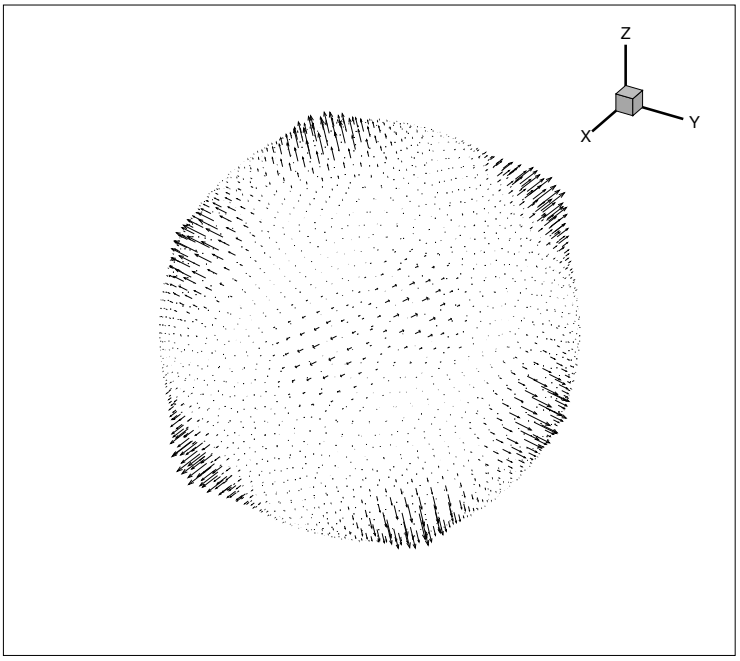

Figure 2.5: Case with eight directions.

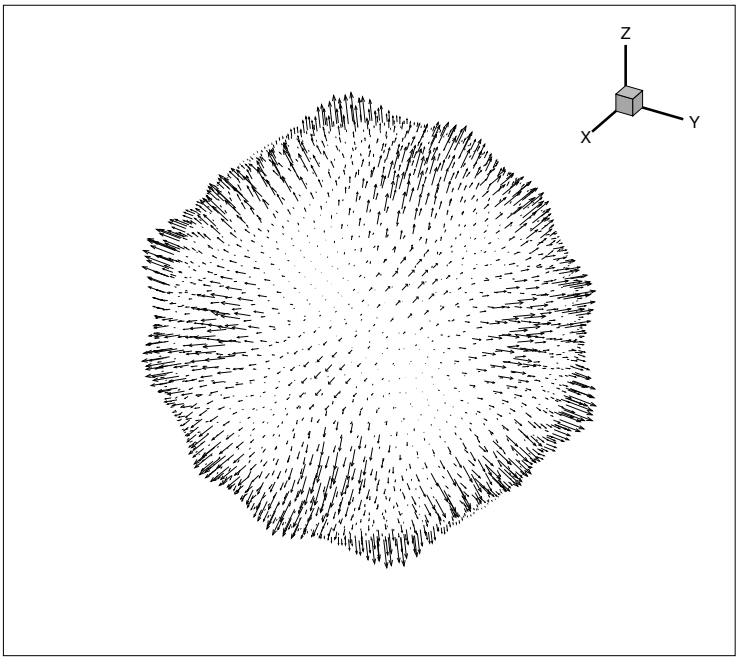

Figure 2.6: Case with 24 directions.

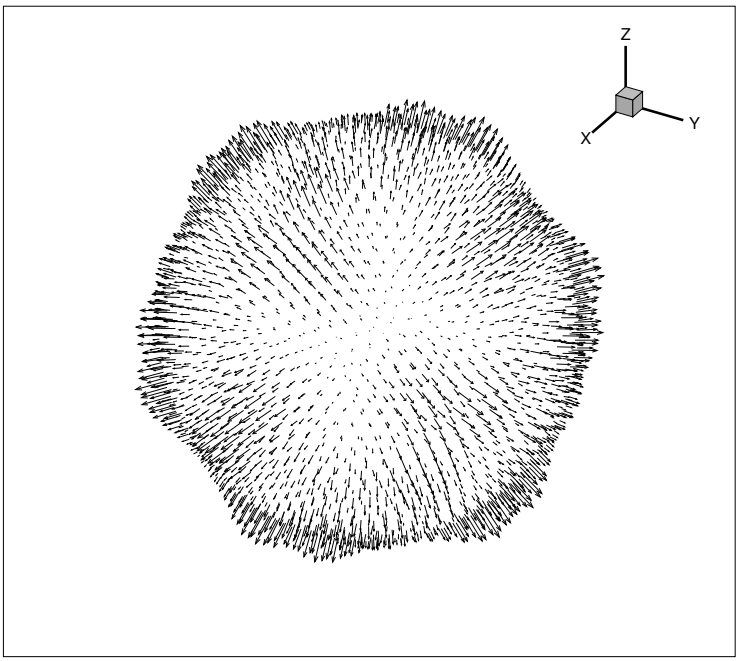

Figure 2.7: Case with 48 directions.

As it was expected, the solution will tend to approximate to a spherical uniform solution as the number of directions chosen increases. This vector-based visualization is a quick graphical manner to observe the influence of the number of directions on the solution, but the actual numerical accuracy variation will be analysed later.

There are several other things that can be changed on the code. To mention just some of them, the mixture of the environment, which has been air over this analysis, the method on the Finite Volume algorithm (exponential or not), the maximum and minimum temperatures, pressure...

To just throw a bit brief of the analysis of these variables on the code, the code is implemented to take the pressure and temperature values from the flow, but to provide a testcase in which an analytical solution could be found, a constant pressure and a gaussian temperature as a function of the radius have been chosen. This temperature distribution can be described as follows:

$$T(r) = T_{max} - (T_{max} - T_{min})\frac{(1 - e^{-(\frac{0.01r}{\Delta T})^2})}{(1 - e^{-(\frac{0.01r_{max}}{\Delta T})^2})} \tag{2.16}$$

where r is the radius of the sphere as a variable, r_{max} is the maximum value of the radius at the boundaries of the sphere, T_{max} and T_{min}, the maximum and minimum temperature values in the distribution and $\triangle T$ the discretization value for the temperature.

The values for the different parameters over the sphere test are:

$$T_{max} = 12000K \tag{2.17a}$$
$$T_{min} = 1000K \tag{2.17b}$$
$$r_{max} = 1.5cm \tag{2.17c}$$
$$\Delta T = 0.0071cm \tag{2.17d}$$

This temperature profile can be better visualized on the following figure:

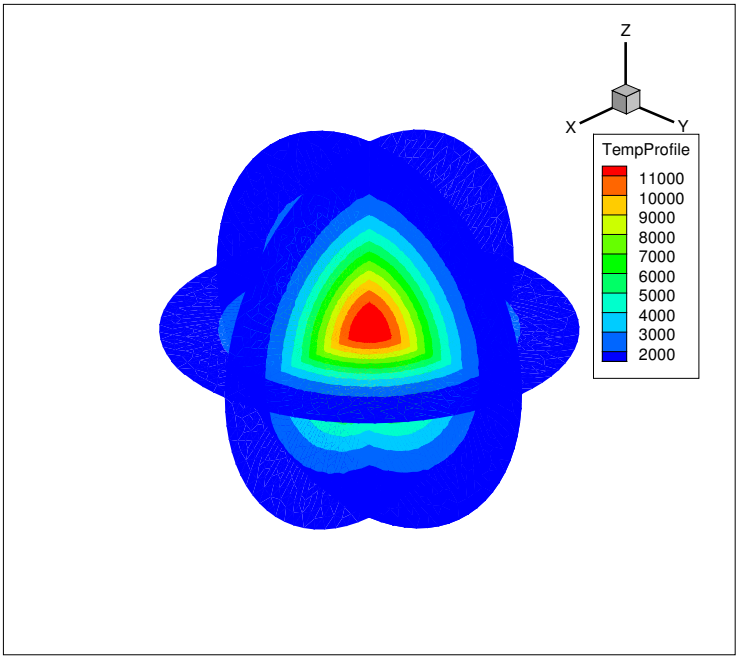

Figure 2.8: Gaussian temperature profile for the studied testcase

2.3.1 Parametric analysis results

The first part of this report was dedicated to present the results of a preliminary analysis of the code. This second part will be more deeply dedicated to report the comparison between more fundamental aspects of the problem, in order to offer a tool to select the best options for computing the radiative properties.

The first case studied is still a sphere, with a Gaussian temperature profile and a constant pressure of ten atmospheres imposed. The meshes used are an unstructured 84000 cells mesh with 100 points in the radial direction and 20 in the azimuthal one and a coarser one

with 22 points for each of the principal directions, as it was stated before.

Two methods to calculate the divergence of the flux are presented as well. The first one, implemented in the base code uses a function implemented in the code which is then multiplied by the weights for each of the directions. The second one, more direct, was implemented directly by use of the direct equation for the divergence of the flux. This applies the same formulation of the radiative transfer equation and the radiative fluxes, equations (2.18a) and (2.18b), but takes directly the formulation for the divergence of the radiative flux stated by equation (2.18c). In any of the cases, the results were found to be equal for both approaches, so we will restrict ourselves to the values provided by 4.7.

$$\vec{\Omega} \cdot \nabla I_\nu = \kappa_\nu (S_\nu - I_\nu), \tag{2.18a}$$

$$\vec{q} = \int_\nu \int_\Omega I_\nu \vec{\Omega} \, d\Omega \, d\nu, \tag{2.18b}$$

$$\nabla \cdot \vec{q} = \int_\nu \int_\Omega \kappa_\nu (S_\nu - I_\nu) \, d\Omega \, d\nu \tag{2.18c}$$

2.3.2 Exponential and non-exponential intensity computation

As it was described in subsection 2.1.1, two methods of adressing the calculation of the radiative intensity following were implemented in the code. The following figures represent the different values for the solution obtained with the use of either the exponential or the non-exponential method. In 2.9, the radiative flux over the radial direction is calculated for 8, 24, 48 and 80 directions, using the exponential method, and for both the coarser and finer mesh (FM).

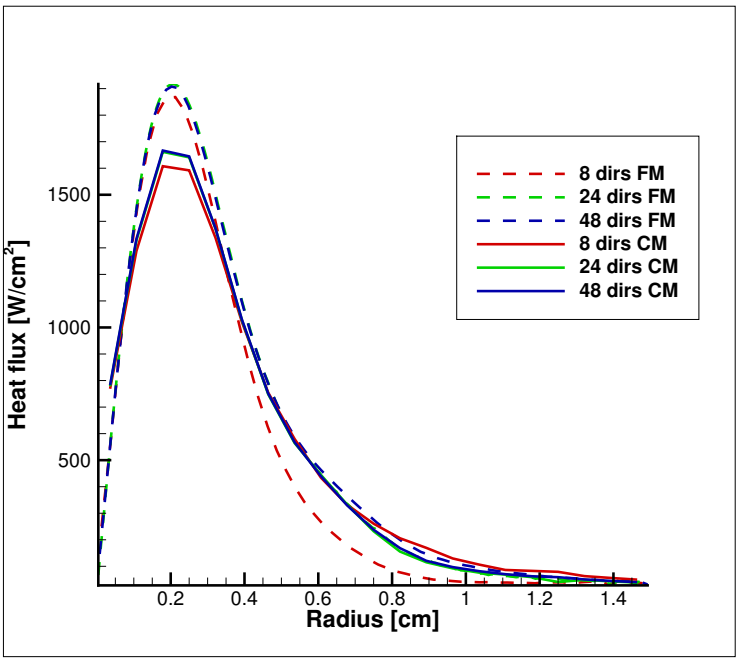

Figure 2.9: Results with the exponential method as a function of the number of directions

We can easily extract some conclusions by looking at the data from the graph. As the number of directions increases, the curves get closer to each other, which means they are presumably converging to the solution. Although the shape of the solution is similar for the two meshes, the peak flux differs between the two solutions on a 13% approximately. The bad accuracy of the coarser mesh can also be seen on the inner part of the sphere, where the solution vanishes due to the low number of integration points. Although the results on the thinner mesh are presumed to be closer to the real solution, this hypothesis has to be demonstrated after against an analytical solution.

Then, the curves are also presented for the non-exponential case, with a behavior for the sphere testcase very similar than in the previous case. The solution is also much smoother in the case of the thinner mesh than in the other case, and, again, the results are converging with the number of directions, being already almost equal for the 24 and 48 directions cases.

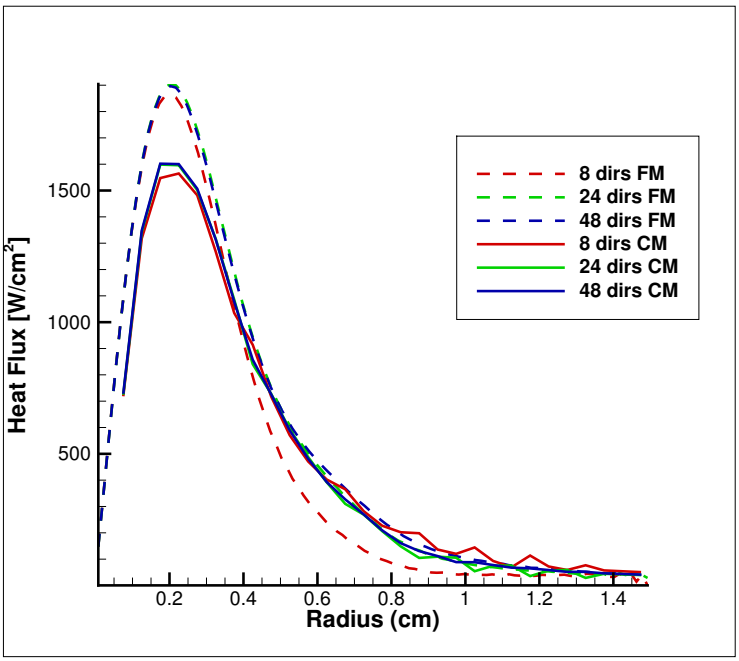

Figure 2.10: Results for the non-exponential method as a function of the number of directions

Finally, both methods are compared, for the case of the thinner mesh, throwing some interesting data as we can see in figure 2.11

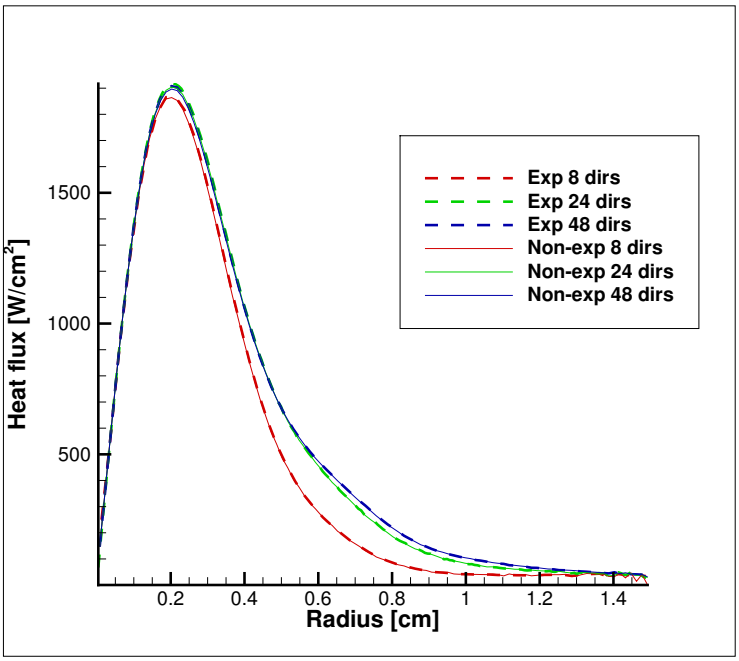

Figure 2.11: Comparison between the exponential and the non exponential method

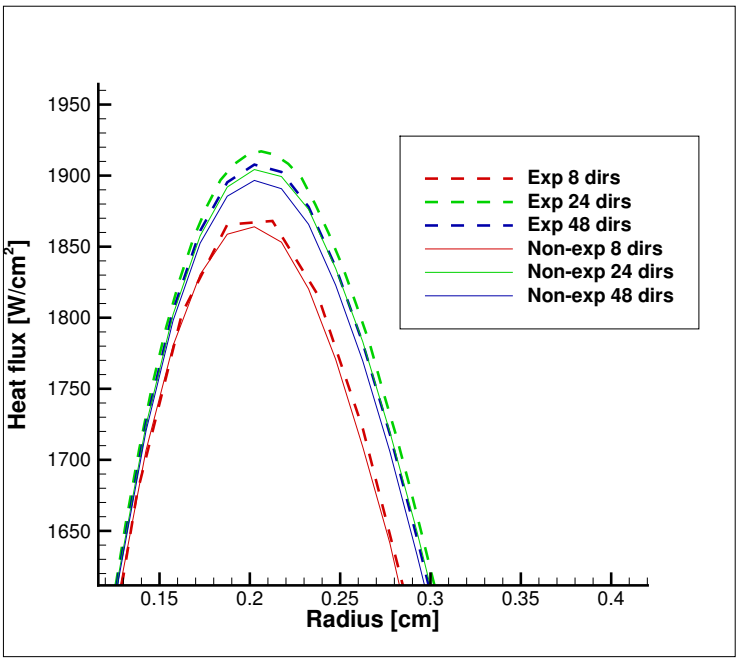

Figure 2.12: Detail on the spherical fluxes on the inner part of the sphere

The two methods show very similar results, being closer than a 1% diference for the case of 48 directions.

In the case of the divergence, figure 2.13 shows the divergence of the radiative flux calculated also for the four direction cases and both exponential and non exponential method.

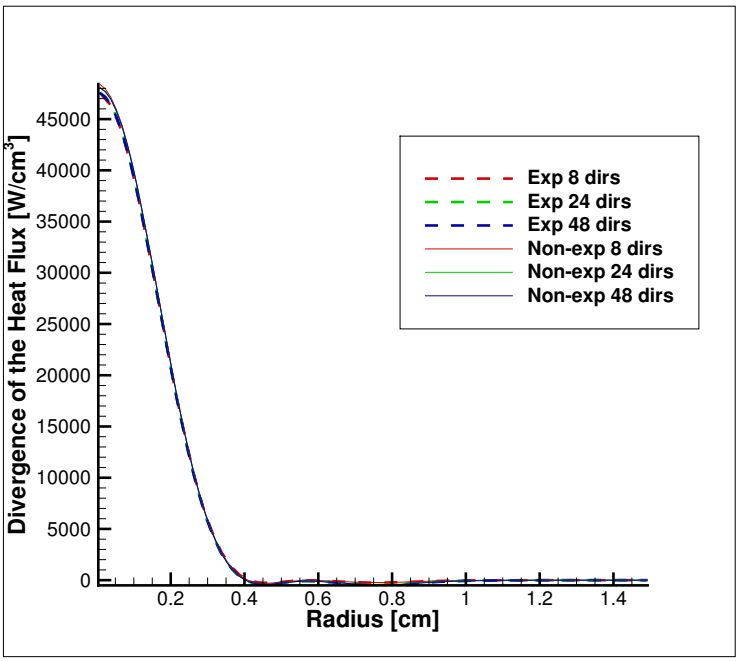

Figure 2.13: Comparison between the exponential and the non exponential method

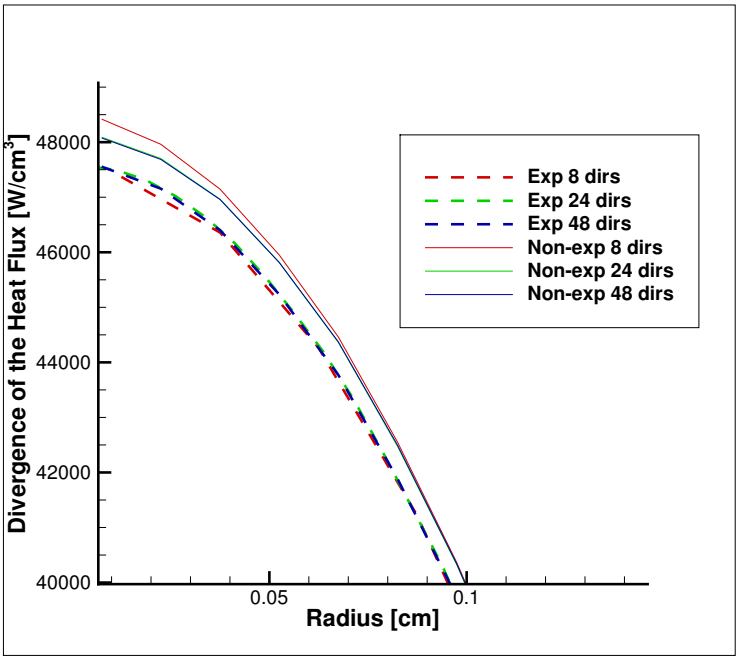

Figure 2.14: Detail on the divergence in the inner part of the sphere

Figures 2.13 and 2.14 confirm the tendency followed by the heat fluxes over the sphere for both methods of adressing the radiative intensity calculation.

2.4 Conclusions from the parametric study

Over the past section, an analysis has been done to try to evaluate the code, optimize the parameters used, and decide what will be the best options to use from now on.

Two methods, the exponential-constant method and the non-exponential one, were implemented in order to compute the radiative intensity needed for the fluxes and their divergences. Although this code needs to be checked on a more complicated geometry, the results are coherent with the theoretical approach. The solution seems to converge when we increase the number of directions, whereas for this simple geometry, the greater accuracy of the exponential method has been impossible to demonstrate. Two methods were as well implemented to compute the divergence, giving similar results. The results were also compared to the ones obtained in [Alvarez 2016], fitting in shape and magnitude.

The following steps would be to perform an analysis on a more demanding geometry, with a mesh that offers greater resolution, and, if possible, with an already tested solution to compare the results, and to solve the 80 directions problem to get a more robust code.

This has been done for three cases, with meshes provided by the DLR. The cases are FireII, Viking, for a martian reentry, and Huygens, for a Titan reentry. These cases are first analysed to see the accuracy of the solution provided, and then modified to be able to handle the new code.

2.5 Verification of the code

The objective to verify the code is not straightforward. Analytical solutions exist only for extremely simple configurations, which differ far from reality, and semi-analytical ones provide a mean to compare the results, but they also introduce a degree of uncertainty in the results.

2.5.1 Spherical case

Nevertheless, the case of the sphere provides a good benchmark to test the Finite Volume code against a semi-analytical solution. This solution has been taken from [Meurisse 2016], with permission of the authors. As the number of directions is increased, the solution tends to approach the analytical one. However, even for the case of the highest number of directions, a 5% difference can be appreciated for the maximum peak flux, although this difference is reduced to less than 1% on the outer part of the sphere. This difference is attributed to three main factors; the mesh, which was chosen as a good input in order to balance the computational time and memory consumed and the accuracy of the results,

the number of directions, which is still not high enough to provide an uniform solution for the fluxes, and to the fact that both the analytical solution and the FV one, depend on the values obtained for the absorption and emission coefficients for air. If these values differ, the solution will then differ with them. In the case of the divergence of the flux, no great differences can be appreciated in the sphere case, as it can be seen in fig 2.15.

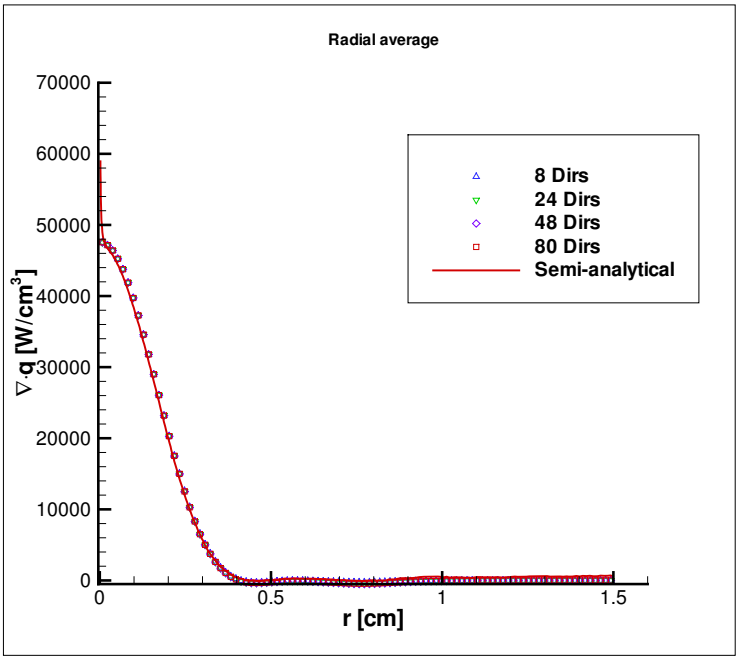

Figure 2.15: Comparison of the radiative divergence of the flux with the semi-analytical solution

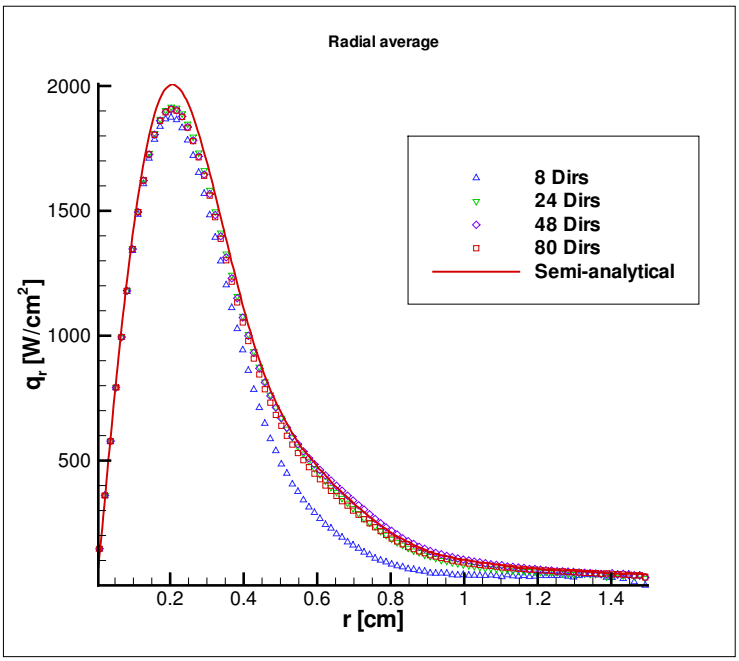

Figure 2.16: Comparison of the radiative radial flux with the semi-analytical solution

2.5.2 Cylindrical case

Another testcase has been chosen in order to improve the verification of the code. In this case, the benchmark has been a cylindrical 3D configuration, which has been created in order to reproduce the conditions of reference [Scoggins 2013]. The geometry, as well as the conditions of the simulation, are expresed in table 2.2:

The temperature profile chosen is a Gaussian temperature profile, whose shape simulates a high pressure arc-column, that usually have a hot core which then is cooled as the flow reaches the outer region, cooler.

$$T(r) = (T_{wall} - T_{max})[\frac{exp(-(\frac{(r/R)^2}{2\sigma^2}) - 1}{exp(\frac{-1}{2\sigma^2}) - 1}] + T_{max} \tag{2.19}$$

This temperature distribution depends on three factors, the maximum temperature T_{max}, the temperature at the wall T_{wall} and a parameter σ which represents the variance of the gaussian profile. Two testcase conditions have been represented and compared. The conditions for these three parameters are represented in table 2.3.

Several meshes were used for this testcase. Both, coarse meshes were created to test the simulation, but the results were, as expected, diverging on a non-despicable amount from the original. The fact of doing an structured or non-structured mesh has been considered,

Geometrical properties	
Radius of the cylinder(cm)	1.5
Length of the cylinder(Nb of radius)	20
Physical properties	
Flowfield conditions	Local Thermodynamic Equilibrium
Flow composition	Air, 11 species
Radiation solver	Tables opacity binning (100 bins)
Pressure P_∞ (Pa)	101325
Temperature T_∞ (K)	Gaussian profile
Computational configuration options	
Number of directions considered	48
Use of exponential method	true
Post-processing software	Tecplot

Table 2.2: Cylindrical simulation conditions

Case	T_{max}	T_{wall}	σ
Case 1	12000	1000	0.33
Case 2	10000	1000	0.66

Table 2.3: Gaussian temperature profile parameters

but finally, and considering the skewness of the mesh elements, an unstructured mesh with more than three and a half million elements.

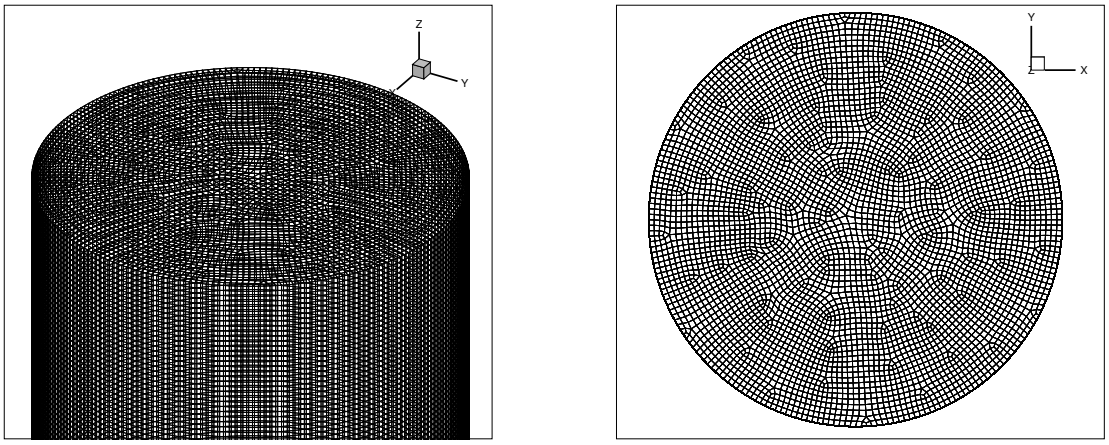

(a) Mesh structure (b) Detail on the upper cylinder boundary

Figure 2.17: Cylindrical mesh used for the simulations

This mesh will presumably capture well the conditions on the constant z planes, where the temperature profile is variable. An almost 2D cylindrical structure could have been chosen for this testcase, as the temperature does not vary along the length of the cylinder, but the structure of the mesh has been created to test as well the results on the second part of the article, where the temperature does vary along the z coordinate.

The comparison between the solutions for the divergence of the radiative heat flux is presented in fig 2.18

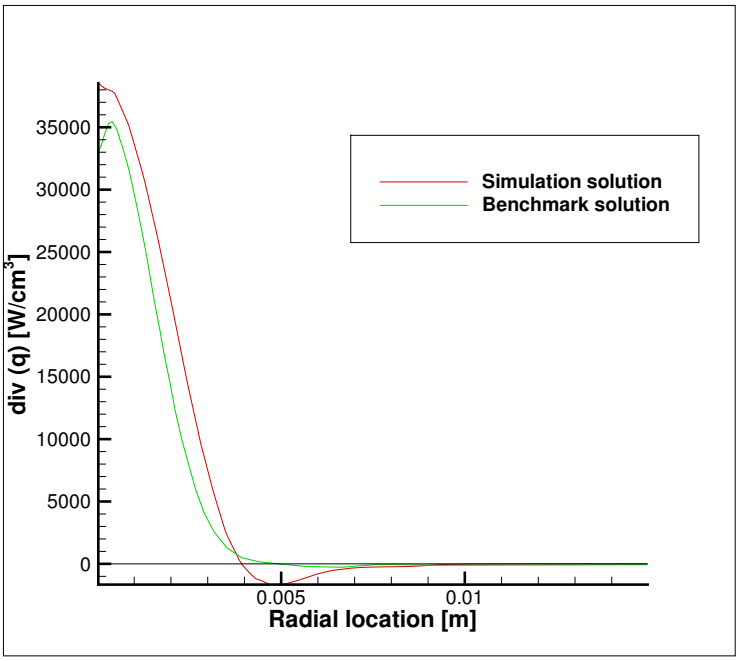

Figure 2.18: Comparison of the divergence of the radiative heat flux for the cylinder testcase

The maximum error between the solutions reaches a 7 % on the peak of the divergence, and can be attributed to several factors. The main one is the variance of the parameter σ on the gaussian temperature distribution, which was adapted to fit the gaussian profiles in [Scoggins 2013], as the value in the article was found to not match this curves. Small differences in the core temperature may lead to great differences in the divergence. Second, the boundary conditions, which were not found, and which assumed then the cylinder walls to behave as a black body object. And finally, slight changes in the air mixture composition (air with 11 species in this case), may lead as well to small differences on the solution.

Chapter 3

Spectral computations

3.1 Calculation of the spectral properties

Equations (2.5) and (2.12) provide a solution for the spectral intensity, but they depend on two spectral quantities; the absorption coefficient and the source term.

The original base code computed the radiative properties, these are, the absorption and emission coefficients, by interpolation from a table which 100 bins and several temperatures, obtained from the NEQAIR NASA software. This limits somehow the performance of the code (air mixture, fixed number of bins, interpolation), so the focus was put on being able to interface a software to be able to perform any kind of test desired.

The software chosen has been then PARADE, a software developed for the European Space Agency [Smith 2010], which allows similar features than NEQAIR, HTGR or other similar radiation databases. Starting with a base interface developed by Lani and Santos at VKI [Santos 2016], it was modified to reduce the computational time by introducing a multi-spectral approach that groups the spectral properties instead of performing a LBL computation on the FV solver. Several mixtures were created in order to test cases in Earth, Mars and Titan. Table 3.1 provides an overview of these mixtures and the elements that must be present to perform correctly the calculations.

3.2 Spectral analysis

The input files needed by the software are the grid, which contains the spatial data of the elements in the mesh, and two additional grids; one temperature grid, with the temperature values data on the elements and a density grid, with the data of the partial densities of the species present in the mixture for each of the elements of the cell. PARADE takes then the input files with the desired mixture and the mesh file and obtains the data for

Spacecraft	FireII	Viking	Huygens
Mixture	air11	CO25	CN
	N_2	CO_2	CN
	O_2	CO	
	NO	O_2	
	N	C	
	O	O	
	N_{2+}		
	O_{2+}		
	NO_+		
	N_+		
	O_+		
	e^-		

Table 3.1: Mixtures used for the reentries calculation

the absorption and emission coefficients for each cell and each wavelength.

It has already been discussed in section 2 the importance of the number of directions or the use of an exponential or non-exponential approach to solve the Radiative Transfer Equation. Similarly, there are two main factors which play a fundamental role on the computation of the absorption and emission coefficients, which are the number of spectral points considered and the number of elements present on the radiation computation.

Over the next pages, a sensitivity analysis has been perform to understand the effects of the variation of these two configuration options on the solution, and to be able to select an appropriate configuration for the analysis which are carried out later.

Three main testcases have been created and analysed for this study. The first of them, the Fire II spacecraft testcase, will be further explained in chapter 4. The spacecraft had a blunt body configuration, similar to the Apollo type capsules, and performed an Earth reentry. The other two, Huygens and Viking, were spacecraft which targeted Titan and Mars, respectively. Over this work we will restrict ourselves to the solution obtained for the Fire II testcase, although information and results for similar radiation analysis with Huygens and Mars can be found in [Potter 2013], [Mazoué 2005] and [Karl 2013]. Table 3.1 contains, as a mode of comparison, the elements used for the flowfield solution on the three testcases.

The accuracy of the solution for the radiative computations depends on the correct mod-

elisation of the radiative spectrum. This depends on its behalf on the selection of a highly enough number of computational points over the wavelength range. Few number of points may lead to totally different solutions, as it is shown in figures 3.1 and in 3.2, which show the absorption and the emission spectrum, respectively, for two different points discretizations: 50 and 10000 points, and for a simple testcase performed with the PARADE database. It can clearly be seen that the error introduced is non-negligible for every point in the spectrum, and it can reach more than a 50 % for some of the points. If the number of points is increased, the solution converges as it is shown in figure 3.3. These results show the variation of the spectral properties on a simple configuration, nevertheless, real testcases require a number of points which may oscillate between a hundred thousand points and millions [Karl 2011], [Lopez 2013].

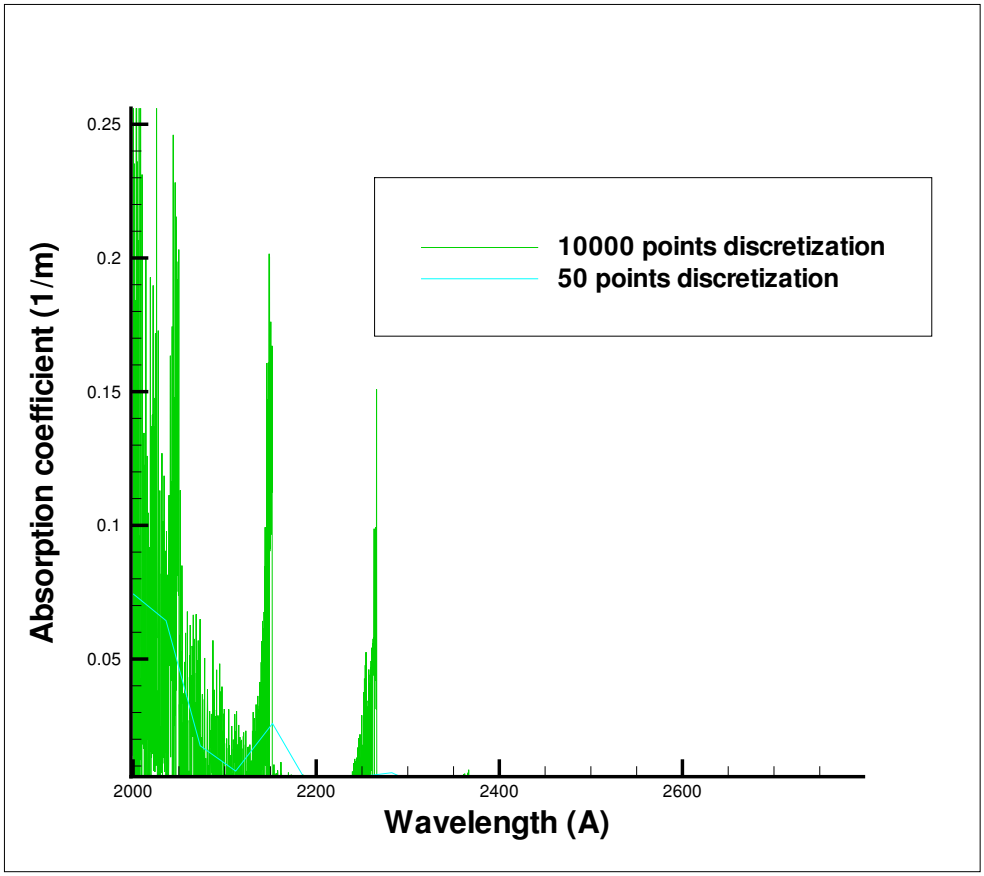

Figure 3.1: Detail of the comparison of the absorption spectra, FireII testcase

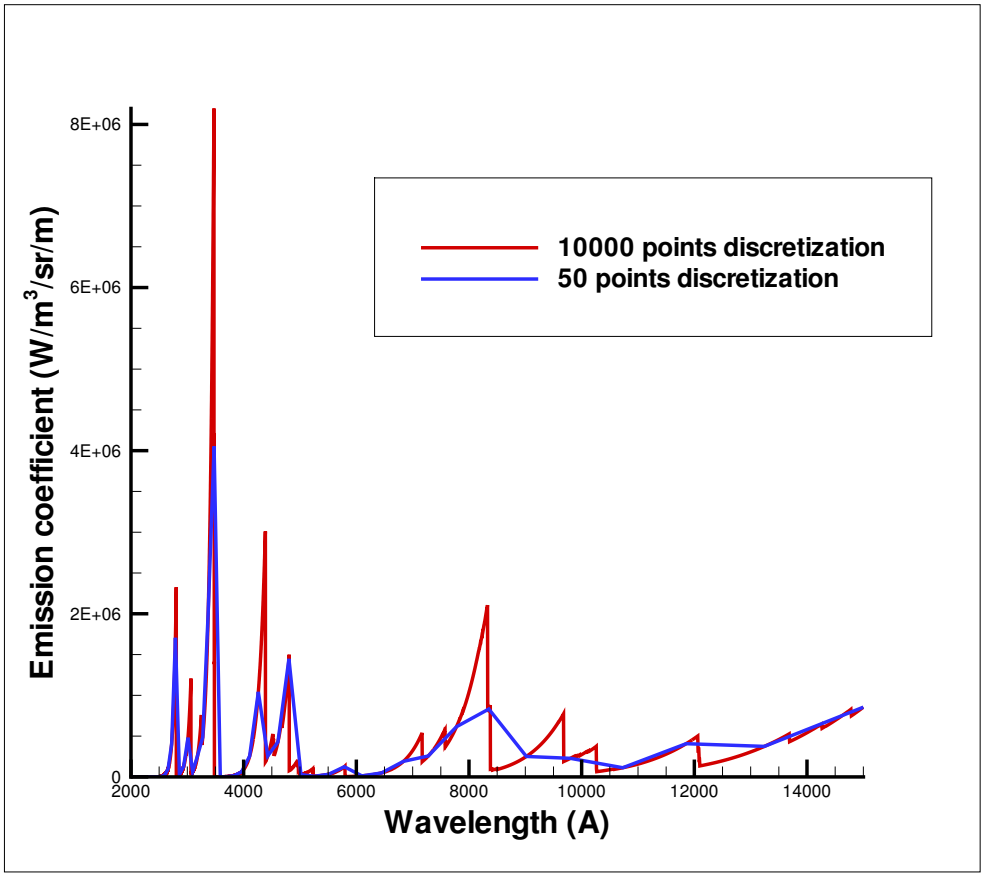

Figure 3.2: Comparison of the emission spectra, FireII testcase

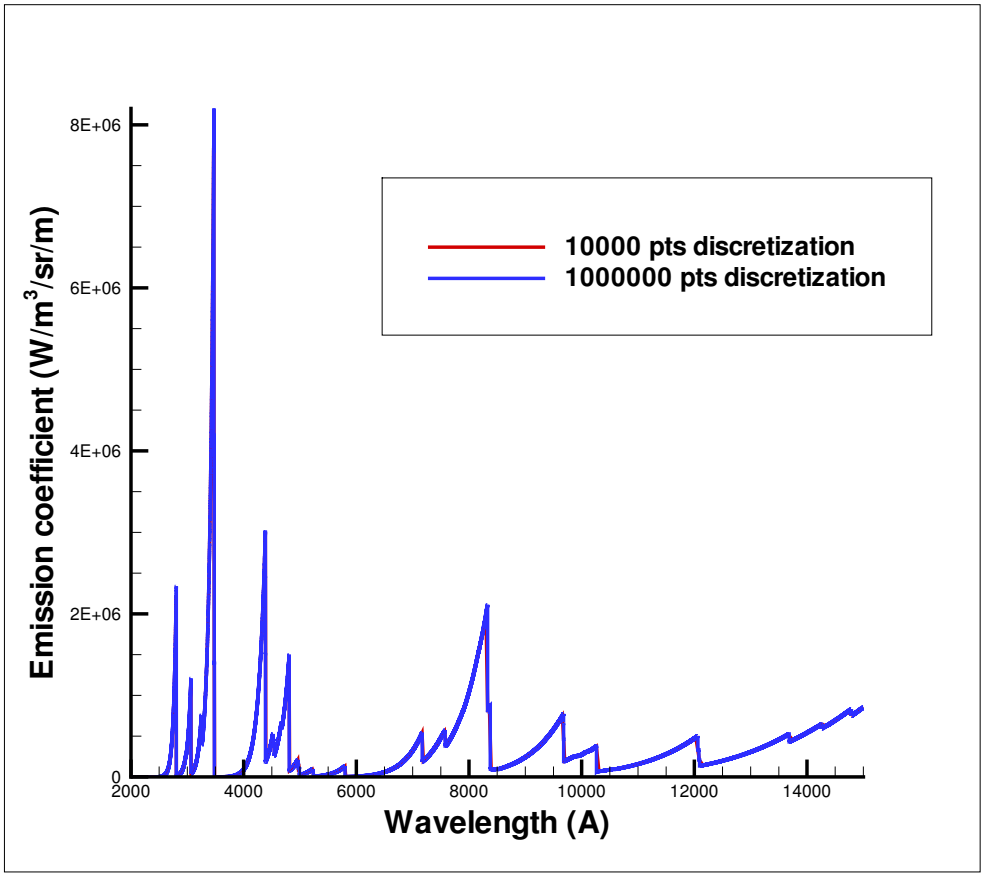

Figure 3.3: Comparison of the emission spectra, FireII testcase

Although the number of spectral points drives the accuracy of the solution, the behavior of the spectrum is driven by the species considered, which provide the atomic and molecular radiation needed for the computation of the coefficients. Not including some of them, may also lead to solutions which differs notably to the exact one. An analysis has been done to see the influence of the main air radiators over the wavelength range. The elements which have been considered for the analysis are the ones that will be used for the flux computations, these are, N, O_2, O, NO, N_{2+}, N_+, O_+ and N_2. The electronic species have been omitted of this analysis because no great difference on the absorption and emission spectrum has been observed by including them or not. Very important conclusions can be extracted by looking at figures 3.4 to 3.9. It can clearly be seen that some of the elements, as the $O+$ component and the $N+$ component drive the shape of the emission spectrum, whereas others like O_2 or NO have a greater influence on the absorption one. It is not the objective of this work to provide a detailed description of the atomic and molecular transitions that drive this results, but the interested reader can read [Smith 2010] and appendix C to gain a further understanding of this results.

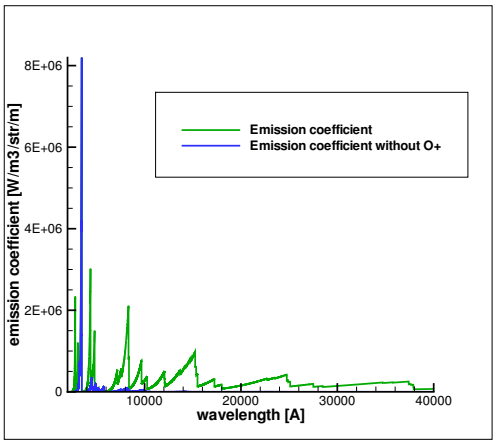

(a) Emission spectrum with and without the O+ component

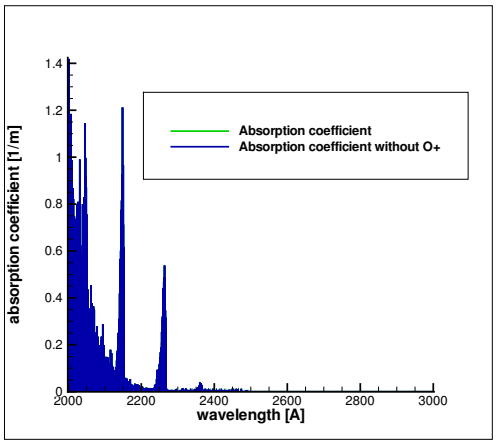

(b) Absorption spectrum with and without the O+ component

Figure 3.4: Influence on the spectrum of the O+ component

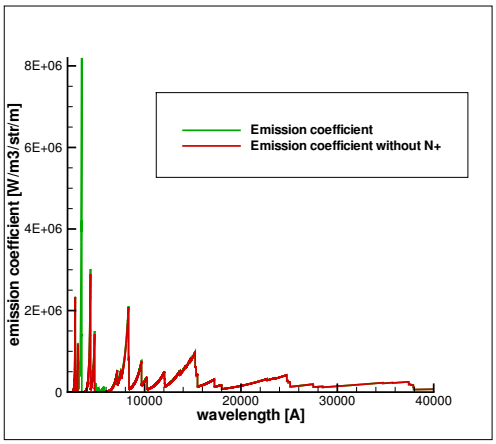

(a) Emission spectrum with and without the N+ component

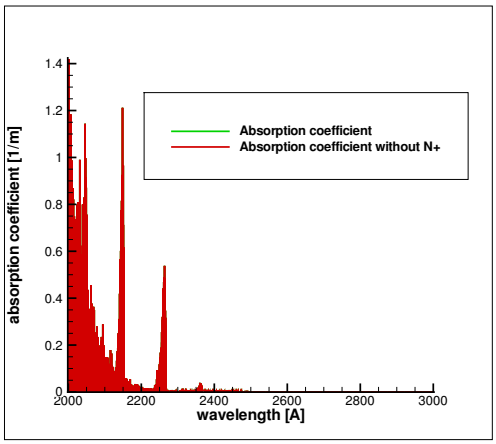

(b) Absorption spectrum with and without the N+ component

Figure 3.5: Influence on the spectrum of the N+ component

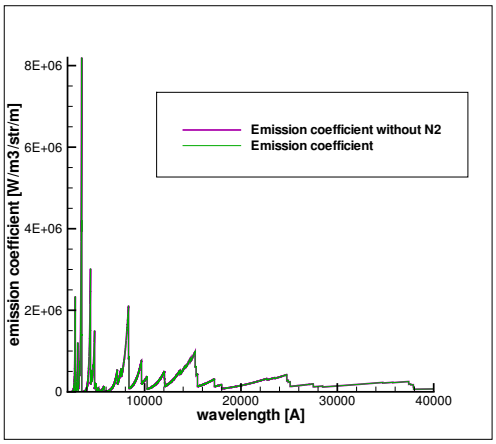

(a) Emission spectrum with and without the N2 component

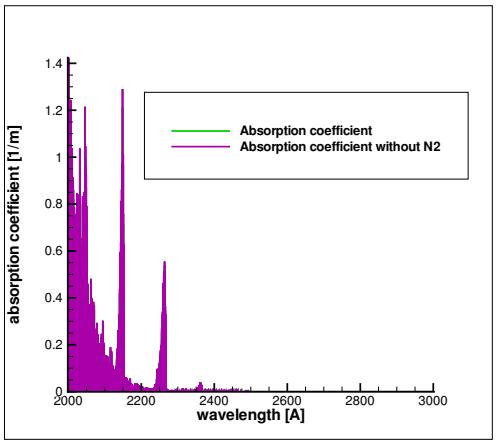

(b) Absorption spectrum with and without the N2 component

Figure 3.6: Influence on the spectrum of the N2 component

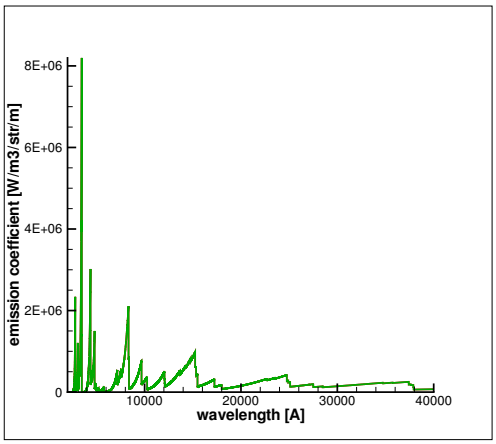

(a) Emission spectrum with and without the O2 component

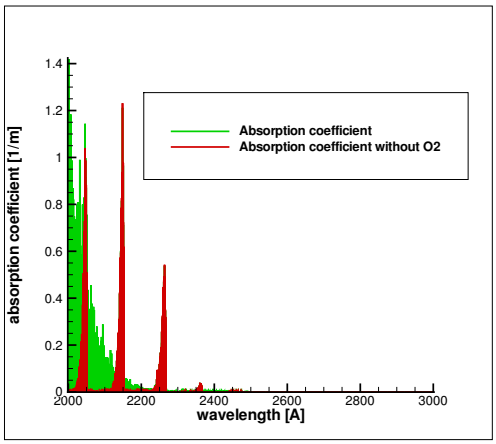

(b) Absorption spectrum with and without the O2 component

Figure 3.7: Influence on the spectrum of the O2 component

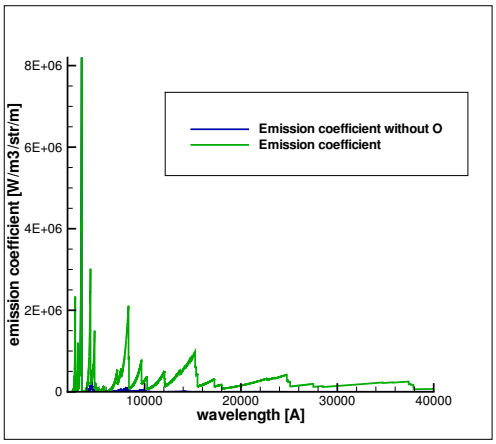

(a) Emission spectrum with and without the O component

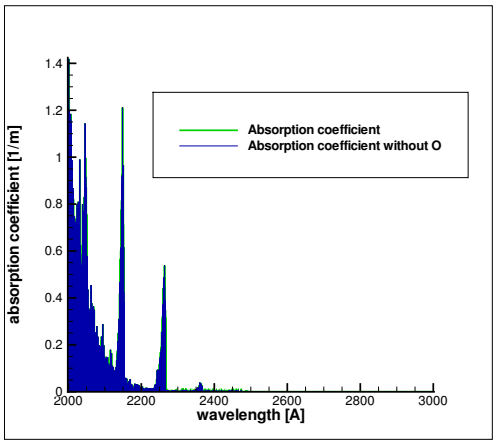

(b) Absorption spectrum with and without the O component

Figure 3.8: Influence on the spectrum of the O component

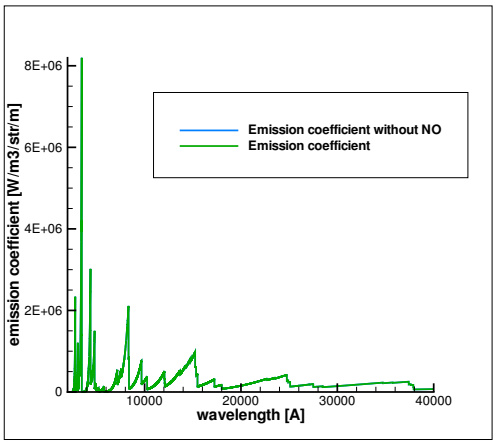

(a) Emission spectrum with and without the NO component

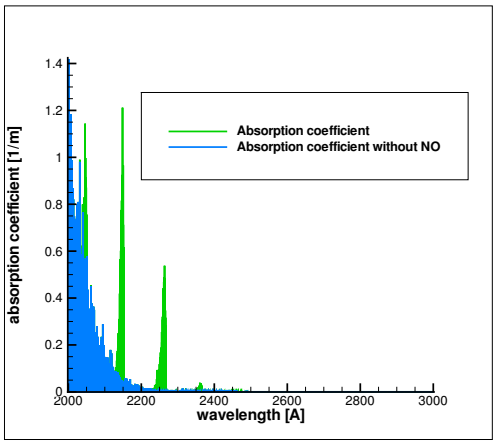

(b) Absorption spectrum with and without the NO component

Figure 3.9: Influence on the spectrum of the NO component

The results provided over this analysis have provided useful information about the configuration options that would need to be introduced on a testcase to consider the results as significant for a real analysis. This testcase has only been used as an example on how the different parameters can lead to a non accurate solution if they are wrongly selected. Usual configurations for air reentries include all of these chemical compounds, and millions of spectral points are considered for the spectral discretization. The memory constraints of the computers used will drive to consider along this work an spectral number of points which does not exceed 2000 points in any of the cases, which will be enough to prove the results qualitatively, but that introduces a great error on the solution with respect to the

real case.

Chapter 4

Multi-spectral approach

In order to achieve accurate results on the resolution of the RTE, the frequency spectral coefficients must be calculated with enough precission. The solver must be able to extract these data from a database, and perform the integration on equation 1.6 in order to find a solution for the radiative intensity. The LBL computational approach is the most used in literature, but it is extremely expensive in terms of memory and time requirements. Another approach is based on trying to find a way to group these spectral properties so that the properties over these smaller number groups can be averaged. These methods are called multi-spectral reduction methods, and we can perform them in two approaches; binning and banding. Approaches of this kind are frequently used in astrophysics, but few reseach has tried to applied them in the planetary exploration field.

4.1 Binning algorithm

The next step in the development of the model has been then to create an algorithm to perform a binning for the opacities, as analysed in [Wray 2006]. To reduce the computational time, the spectra is divided into groups of frequencies, and then into bins which have similar mean opacities.

The absorption and emission coefficients can be found for each cell in the mesh and each wavelength using PARADE, or another radiation database like HTGR. These data is then used to obtain an averaged absorption coefficient, as follows:

$$\alpha(\sigma) = \frac{\int_x S(\sigma, \boldsymbol{x})\alpha(\sigma, \boldsymbol{x})dx^3}{\int_x S(\sigma, \boldsymbol{x})dx^3} = \frac{\sum_{V_{cell}} \alpha_i B_i V_i}{\sum_{V_{cell}} B_i V_i} \tag{4.1}$$

where a discretization of the integrals over the computational volumes is performed to obtain a value of the mean coefficient for each wavelength. The minimum and the maximum values on this vector are found and assigned as the boundaries of the bins, and between

them, the number of bins desired is distributed logarithmically. To set a simple example of this, if a vector of mean absorption coefficients for nine wavelength values is provided:

$$\alpha = [5.4, 4.6, 3.7, 4.2, 3.85, 4.33, 4.43.71, 5.2] \tag{4.2}$$

and this spectrum need to be distributed in 5 bins, between the maximum value, 5.4, and the minimum one, 3.7, the 5 bins are logarithmically distributed.

Then, we distribute the values of the absorption and emission coefficient for each cell and each wavelength on the created bins. For this purpose, we find out to which bin correspond each of them , and then we add the corresponding values of the absorption, emission and source term coefficients to that bin and cell.

To understand better how the method works, a graph has been made with the data of the absorption coefficient for a computational cell in the case of an air mixture in the Fire II case.

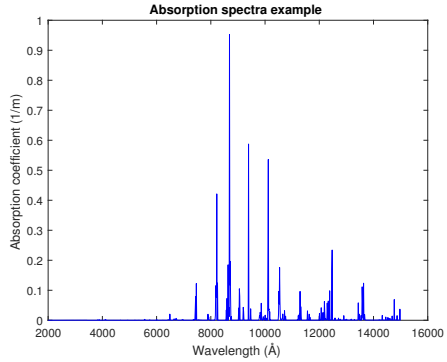

(a) Absorption original spectrum

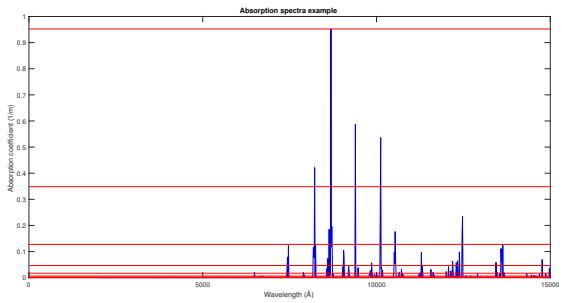

(b) Absorption spectrum binned into 10 bins

Figure 4.1: Example of the binning algorithm method for the case of an air11 mixture

As it can easily be observed in the figure, the bins do not have an equal spacing, but a logarithmic one. This is due to the fact that the number of absorption points in the spectrum is usually much higher at lower absorption values than at higher ones. Equations 4.3 to 4.5 show how the values for the absorption, emission and source term coefficients are incremented on a bin and a cell if the value of the absorption coefficient for a given wavelength and cell is located in that bin.

$$\alpha_{bin,cell} = \alpha_{bin,cell} + \alpha_{cell,\lambda} * B_{T_i,\lambda}; \tag{4.3}$$

$$\epsilon_{bin,cell} = \epsilon_{bin,cell} + \epsilon_{cell,\lambda} * d\lambda; \tag{4.4}$$

$$B_{bin,cell} = B_{bin,cell} + B_{T_i,\lambda} * d\lambda; \tag{4.5}$$

This approach reduces the number of absorption and emission points that are needed for the fluxes computation from N_e times N_{sp} in the beginning, where N_e represent the number of cell elements and N_{sp} represents the number of spectral points, to N_e times N_b, where N_b is the number of bins, whose value is much lower. Supposing that we have a mesh with a hundred thousand points, and that we want to perform an accurate calculation, at least one million of spectral points will be needed to perform a line-by-line method, while with a hundred bins we will already obtain an accurate solution.

Once we have the values for the absorption and emission coefficients for our mesh and number of bins, we can then compute directly the radiative flux and its divergence.

The radiative flux can be computed then as:

$$\vec{q}^{rad} = \sum_{x=1}^{N_b} \sum_{y=1}^{N_d} \sum_{z=1}^{N_e} a_d I^d_{\sigma,e} \vec{\Omega}_d \tag{4.6}$$

$$\nabla \cdot \vec{q}^{rad} = \sum_{x=1}^{N_b} \sum_{y=1}^{N_d} \sum_{z=1}^{N_e} \frac{a_d I^d_{\sigma,e} \vec{\Omega}_d \cdot \triangle \vec{S}_e}{V_e} \tag{4.7}$$

where N_b, N_d and N_e represent the number of bins, number of directions and number of elements, V_e is the volume of each of the computational cell elements, a_d is the weight assigned to the directions Ω and $I^d_{\sigma,e}$ can be obtained from (2.5) or (2.12). Equations 4.6 and 4.7 sum up all the work performed until now. In them, the solution is obtained by summing the contribution of all the elements, along all the considered directions, for all the bins in which we want to discretize our spectral properties. More information on how this equations are computed can be found in appendix A.

4.2 Banding algorithm

The reordering of the spectral properties into bins considering their absorption coefficient is considered to be the most respectful with the physical meaning of the problem. There is nevertheless another approach to follow to reduce the computational cost of the solution, and is to perform a multi-group splitting of the spectral properties. In this case, instead of dividing the spectra into bins, created from the mean absorption coefficient as it was described in equation 4.1, the spectra is divided into bands, simply by splitting the frequency spectra into the desired number of bands.

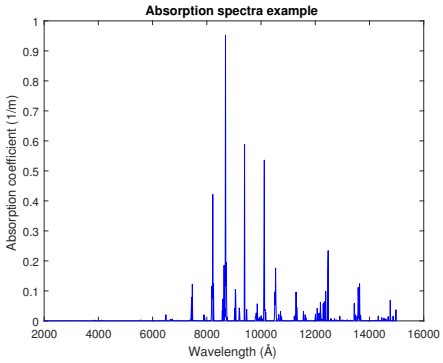

(a) Absorption original spectrum

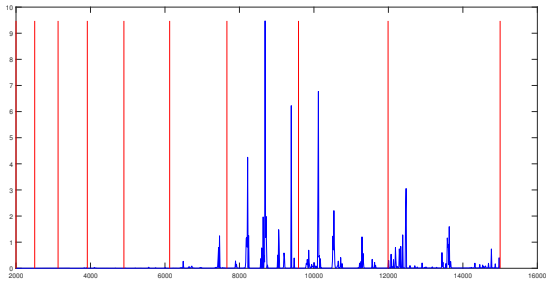

(b) Absorption spectrum binned into 10 bands

Figure 4.2: Example of the banding algorithm method for the case of an air11 mixture

This approach is much more simple, and it requires less memory and computational time to be computed, but a greater number of bands than bins are needed to approach the convergence of the solution.

4.3 The FIRE II testcase

The FIRE II experiment, which flew on the 22nd May 1965, has been used as a testcase to validate the multispectral approach algorithm. The experiment was intended to be a benchmark to analyze the impact of the radiative heating during an Earth reentry, and it provided valuable data to be able to compare with the CFD computations.

The data for the FIRE II experiment testcase, as shown in [Santos 2016] is resumed in the following table:

Test conditions									
Time from launch (s)	1643								
Altitude (km)	53.04								
Speed u_∞ (km/s)	10.48								
Mach number M_∞	31.4								
Density ρ_∞ ($10^{-04} kg/m^3$)	7.8								
Pressure P_∞ (Pa)	62.04								
Temperature T_∞ (K)	276								
Wall temperature T_w (K)	640								
Physical solver									
Flowfield solution	DLR input flowfield solution								
Flow composition	Air, 11 species								
Radiation solver	PARADE								
PARADE settings									
Chemical species	N	O	N_2	NO	O_2	N_{2+}	N_+	O_+	e^-
Spectral band	[2000,40000] Å								
Spectral discretization	Equal frequency increments								

Table 4.1: FIRE II experiment parameters

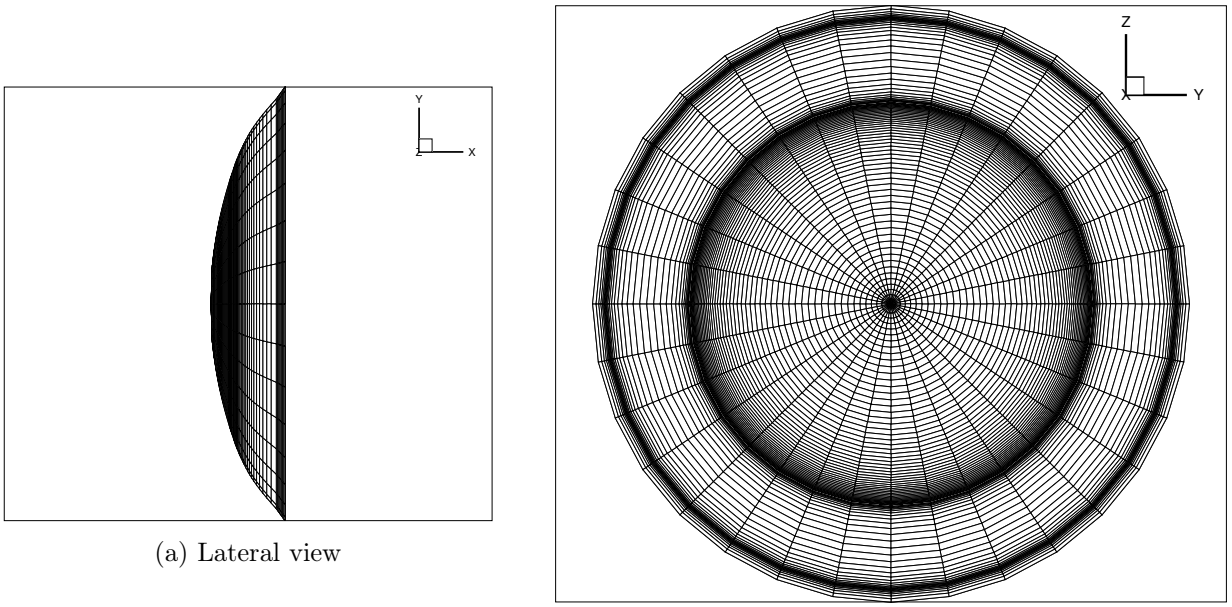

(a) Lateral view

(b) Front view

Figure 4.3: Lateral and front view of the FireII mesh used, inviscid testcase

The mesh used for the Fire II inviscid simulations is shown in figure 4.3. It is a 64 x 32

Number of spectral points	
Use of exponential method	True
Number of directions considered	80
Number of bins considered	Variable
Number of bands considered	Variable
Post-processing software	Tecplot

Table 4.2: Fire II specific computations conditions

cells mesh in the tangential and normal directions respectively.

4.3.1 FireII results

The results obtained with the multi-spectral approach developed are presented in this section for the FireII case. The divergence of the radiative flux, which provides the magnitude of the amount of radiative energy over a volume unit in the flux, is presented for a 100 bins configuration in figure 4.5, and then compared with the solution for the same conditions obtained with a Monte Carlo method using 10000 photons per cell [Santos 2016]. Figure 4.4 shows the distribution along the stagnation streamline of the pressure and temperature fields, which are obtained on the flowfield solution.

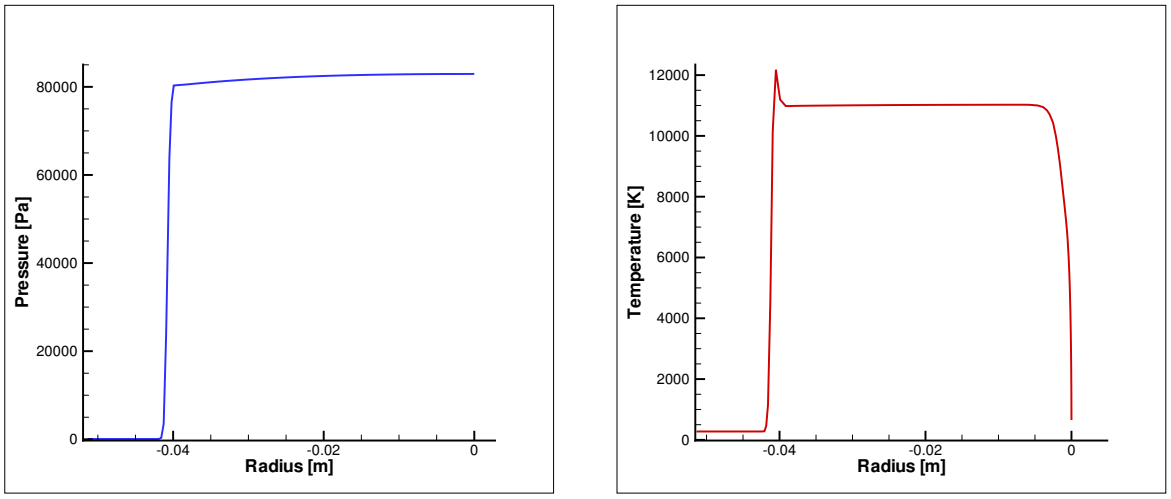

(a) Pressure distribution

(b) Temperature distribution

Figure 4.4: Pressure and temperature distributions along the stagnation streamline, DLR flow solution

The results for the radiative transfer computations are shown on the following figures. Figure 4.5 shows the distribution of the divergence of the heat flux obtained for the viscous

Fire II testcase, by using a hundred bins for the discretization. Figure 4.6 shows the comparison of the solution between the Finite Volume solver and the Monte Carlo one.

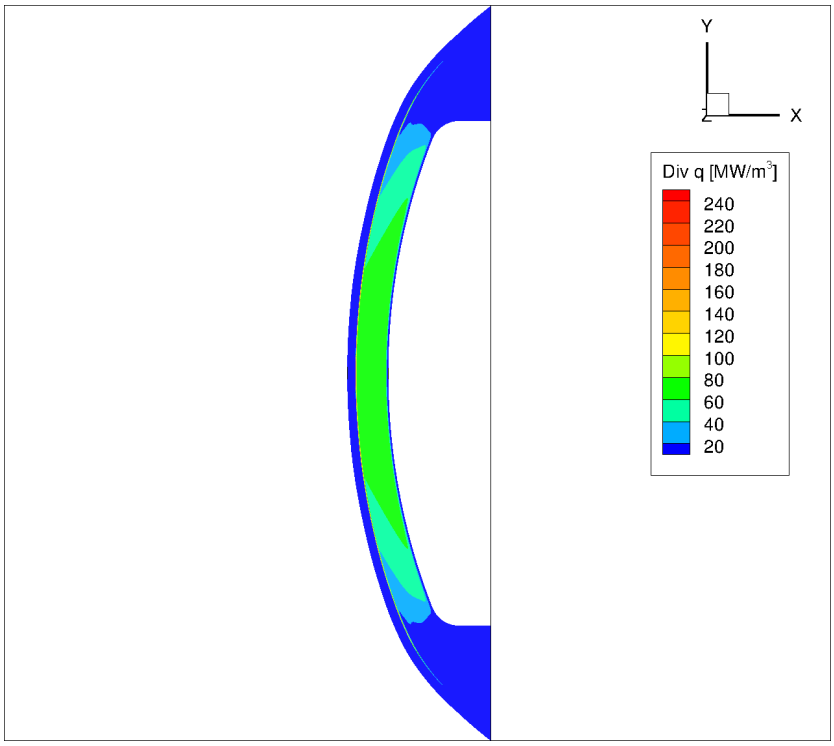

Figure 4.5: FireII divergence results for a hundred bins

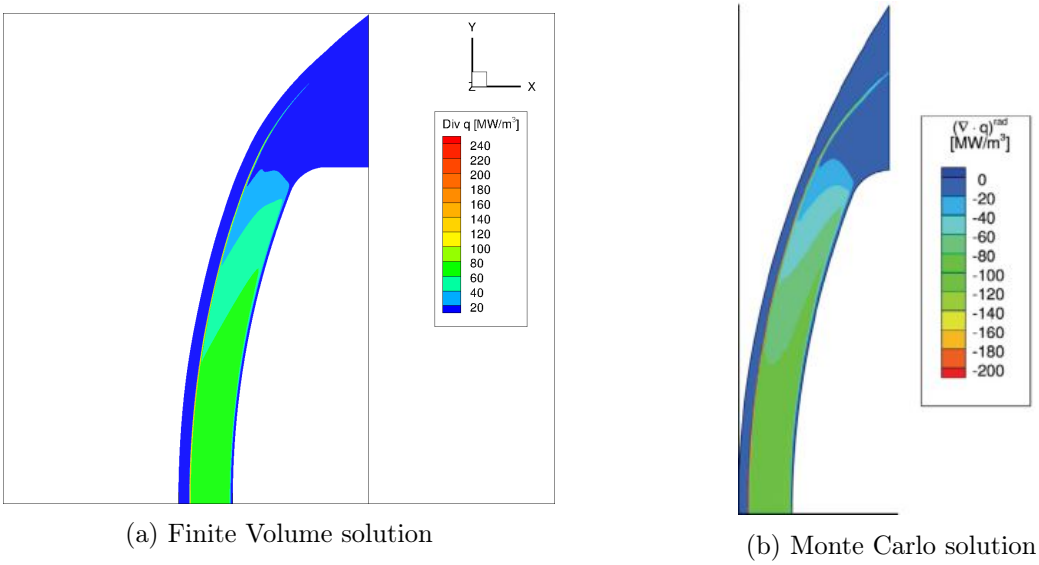

(a) Finite Volume solution

(b) Monte Carlo solution

Figure 4.6: Comparison between the results for the divergence of the flux

Figure 4.6 shows the results for the FV method and the MC for the divergence of the radiative heat flux in the Fire II testcase. This results show a great similarity, but again, emphasis must be put that this testcase can only prove that the physical meaning of the problem is respected, not that the method is providing a close result to the real solution. Research papers like [Göbel 2012] show that for the number of points used, 1000 points, the results may differ for the heat fluxes on more than a 50 % with respect to usual discretizations of hundreds of thousands or million of spectral points. The great dependence of the spectrum with this parameter has already been demonstrated in Chapter 3.

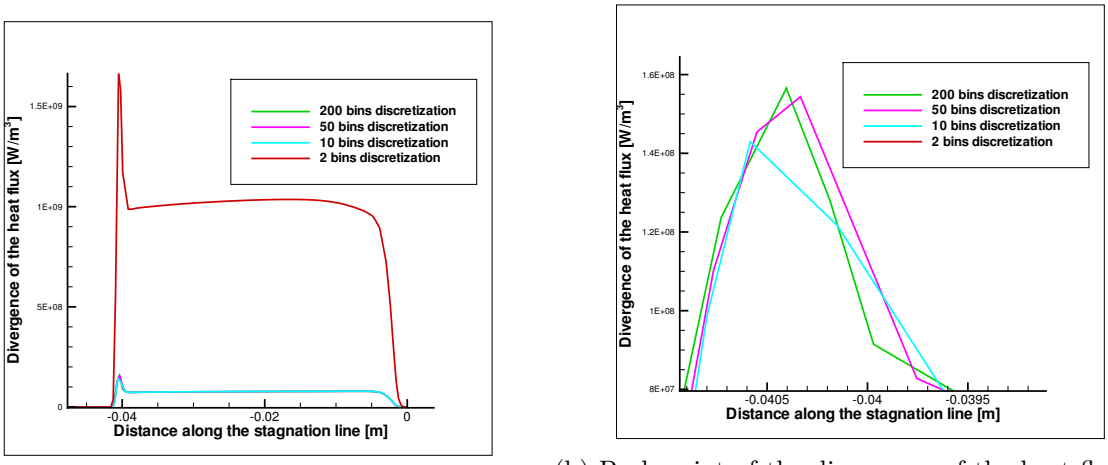

(a) Divergence of the heat flux

(b) Peak point of the divergence of the heat flux solution

Figure 4.7: Radiative heat flux divergence

Figure 4.7 shows the divergence of the heat flux for four different number of bins along the stagnation line. As the number of bins increases, the solution tends to converge as it is shown in 4.7b. An extremely low number of bins like the case of a two bin discretization can produce a relative error close to a 10% between the two solutions. If the number of bins is increased to 10, the relative error decreases for this case to less than a 1%. This fast convergence with the number of bins is coherent to the work done by Wray in [Wray 2006], and by the work performed in astronomy and astrophysical research, like the studies perform by Vogler et al. in [Vogler 2004].

Conclusions

The main objective of this thesis was to generate and test an approach to compute the radiative properties for an spacecraft re-entry configuration on an efficient manner. In the first part, the Finite Volume code was verified against a semi-analytical solution for an spherical testcase with a gaussian temperature profile. The numerical computed solution depends on the angular discretization, providing a better solution as the number of directions was increased. However, for this simple testcase, no substantial difference has been found among the cases with more than 24 directions, as the radiative field solution has a spherical symmetry. Although the exponential method to compute the radiative intensity was created to provide better results than the non-exponential one, the difference was small for this testcase for the same reason than the quick convergence of the number of directions. The number of radial points for the analysis was also chosen by providing a balance between the accuracy on the solution and the lost of the physical meaning of the problem.

The second part of this thesis was dedicated to the study of a multi-spectral approach to interface a radiation library, PARADE, and compute with it the radiation properties for a wide range of mixture configurations. This development increases the range of applicability of the code to different compositions and conditions, providing a greater flexibility for the future research. The results for the Fire II spacecraft showed a convergence as the number of bins was increased. Nevertheless, the results between the Monte Carlo analysis and the Finite Volume, which showed a notable agreement qualitatively, must be compared with a much higher number of spectral points, as literature reveals that this number of spectral points is clearly insufficient to perform accurate estimations of the radiative heat fluxes. Greater effort must be devoted to the validation of the results using a tangent slab approximation, and on the further improvement of the memory requirements of the code, which may allow to run cases with a greater number of spectral points and bins for comparison.

There are several branches that can be followed to continue the work performed over this thesis. The first one is to perform fully coupled flow-radiation simulations for the Finite Volume solver, which would approximate the results to the real flight solution. The radiative problem drives the computational cost of the problem, and the flowfield can be coupled by introducing in the energy equation the divergence of the radiative flux, which

was already computed on this work. This is a previous step for coupling these two physical problems with the ablation chemical products which are detached from the TPS on modern spacecraft configurations, and which would lead to the closest to reality solution possible for the code, but also to much higher computational time requirements.

The second approach, already in progress, is to include an Statistical Narrow Band approach to reduce the time of the computation of the spectral properties. PARADE, and other radiation libraries, use an LBL approach as the main solving system, which increments the computational time drastically. The averaging of the absorption and emission coefficients from the beginning would lead to a further decrease of this time.

Future work

4.4 The Hybrid Statistical Narrow Band approach

The computation of the radiative fluxes based on a multi-spectral approach binning reduces significantly the amount of computational time consumed, as it was stated in chapter 4. Nevertheless, the amount of time necessary to perform the absorption and emission coefficients computation still requires a great effort and consumption of resources. This computational time can be further improved by reusing the data generated from PARADE for future computations, but this limits the scope to simulations performed with the same number of spectral points and mixture properties. But there is another approach that can be taken to reduce the line-by-line calculations over the spectrum. This chapter, which is dedicated to the description of the Hybrid Statistical Narrow Band method and its implementation procedure has been added as additional information on the natural continuation of this thesis, which has already been started, and which will allow to further improve the results over this work.

The state-of-the-art method to approach radiative reentries computation is the LBL method, which discretizes the whole spectra into individual elements, whose radiative properties are then computed. This approach produces very accurate results, but results in high computational time, specially if the considered wavelength range is high, as is needed in most of the reentry spacecraft configurations. To reduce the computational time, we can treat the problem as if it had two different systems; The atomic line radiation, which will still be treated on a line-by-line approach, and the molecular systems and continua, which will be treated with the SNB approach. Because of these two combined methods to treat radiation, the method is called the Hybrid SNB method. Starting again with the solution for the RTE equation in a non-scattering medium of optical index equal to 1,

$$I_\sigma(s) = I_\sigma(0)\tau_\sigma(0,s) + \int_0^s \eta_\sigma(s')\tau_\sigma(s',s)ds' \tag{4.8}$$

where $\tau_\sigma(s',s)$ is the spectral transmissivity between points s' and s, and can be expressed

as follows:

$$\tau_\sigma(s', s) = exp(-\int_{s'}^{s} \kappa_\sigma(s'')ds'') \tag{4.9}$$

The objective is then to divide the spectra into smaller bands, over which the radiative properties will be averaged. The radiative contributions, as was stated before, are then divided into statistically uncorrelated contributions. We can then write equation (4.8) over a narrow band as follows:

$$\overline{I_\sigma(s)}^{\Delta\sigma} = \overline{I_\sigma(s_0)}^{\Delta\sigma} \prod_k \overline{\tau_\sigma^k(s_0, s)}^{\Delta\sigma} + \sum_k \int_{s_0}^{s} \overline{\eta^k(s')\tau_\sigma^k(s', s)}^{\Delta\sigma} \prod_{k' \neq k} \overline{\tau_\sigma^{k'}(s', s)}^{\Delta\sigma} ds' \tag{4.10}$$

where the index k indicates the different radiative contributions. We must nevertheless remark that the assumption of uncorrelation between molecular and atomic lines is only an hypothesis, but numerical studies have shown that it is valid with an accuracy of 1% [Scoggins].

4.4.1 Box model

The HSNB model used considers an statistical narrow band model for optically thick molecular systems, a box model for thin and continua systems, and an LBL treatment for atomic lines. Then the mean intensity can be obtained by summing up the contribution of all the different intensities calculated with these models. The contribution to the intensity of the box model can be written as:

$$\overline{I_\sigma^{box}(s_j)}^{\Delta\sigma} = \sum_{k \in B} \sum_{i=0}^{j-1} \overline{\eta_\sigma^k \Big|_i}^{\Delta\sigma} \prod_{k' \in S} \overline{\tau_\sigma^k(s_i^*, s_j)}^{\Delta\sigma} \Delta s_i \tag{4.11}$$

where s_i and s_j are spatial points and the absorption and emission coefficients for these systems can be tabulated for selected temperature values of T and T^{ve}.

4.4.2 Line-By-Line model for atomic lines

The weak spectral density of atomic lines force us to treat them on an LBL approach. We can therefore write the contribution of these lines to the mean spectral intensity as:

$$\overline{I_\sigma^{at}(s_j)}^{\Delta\sigma} = \sum_{i=0}^{j-1} \overline{\frac{\eta_\sigma^{at}}{\kappa_\sigma^{at}}\Big|_i (\tau_\sigma^{at}(s_{i+1}, s_j) - \tau_\sigma^{at}(s_i, s_j)}^{\Delta\sigma} \times \prod_{\substack{k' \in \mathcal{S} \\ k' \neq at}} \overline{\tau_\sigma^{k\prime}(s_i^*, s_j)}^{\Delta\sigma} \tag{4.12}$$

And the atomic radiative properties are computed using the Einstein coefficients, A_{ul}, B_{ul} and B_{lu}; respectively related to spontaneous emission and induced emission and absorption of the transition u->l as:

$$\eta_\sigma = \sum_{ul} n_u \frac{A_{ul}}{4\pi} f_{ul}^{se}(\sigma - \sigma_{ul}) hc\sigma \tag{4.13}$$

$$\kappa_\sigma = \sum_{ul} [n_l B_{lu} f_{ul}^{a}(\sigma - \sigma_{ul}) - n_u B_{ul} f_{ul}^{ie}(\sigma - \sigma_{ul})] h\sigma \tag{4.14}$$

where n_u and n_l are the number densities of the upper and lower levels, σ_{ul} is the wavenumber of the transition and f_{ul}^{se}, f_{ul}^{a} and f_{ul}^{ie} are the line profiles associated to spontaneous emission, absorption and induced emission, which can be related to each other at T^{ve} in equilibrium as:

$$f_{ul}^{ie}(\sigma - \sigma_{ul}) = f_{ul}^{se}(\sigma - \sigma_{ul})(\frac{\sigma_{ul}}{\sigma})^3 \tag{4.15}$$

$$f_{ul}^{a}(\sigma - \sigma_{ul}) = f_{ul}^{se}(\sigma - \sigma_{ul})(\frac{\sigma_{ul}}{\sigma})^3 exp(\frac{hc(\sigma - \sigma_{ul})}{k_B T^{ve}}) \tag{4.16}$$

The approach to the problem will be as follows:

- First, an interface has been created to be able to generate an input file for the radiative spectra software developed by Scoggins et al. at NASA AMES. This input file contains the data of the partial densities of the species in the atmospheric mixture, and the values for the vibrational and rotational temperatures, both for each cell point.
- Then, the software is automatically run, generating the data corresponding to the absorption and emission (or source term, if preferred) coefficients for each narrow band and cell.
- Finally, these data is used by the Finite Volume Solver to compute the radiative fluxes and its divergence.

This method allow us to reduce in a non-negligible amount the computational time, as the number of spectral points to discretize is much lower than in the case of a database like PARADE. Moreover, it offers us a certain flexibility, as we can for example, save the spectral data for a certain spacecraft model, and then rerun the simulation changing other parameters, without loosing time in these computations.

Appendices

Appendix A

Discrete Ordinates Method

After finding the solution for the radiative intensities using equations (2.5) or (2.12), the integral part on the flux equations over the whole solid angle range can be substituted by a numerical approximation, by summing up the contribution on the flux of all the directions.

$$\int_{4\pi} \vec{\Omega} I_\sigma(\vec{\Omega}) d\vec{\Omega} \simeq \sum_{i=1}^{n} a_i I_\sigma^i \vec{\Omega}_i \tag{A.1}$$

where a_i are the different quadrature weights for the directions s_i.

The choice of the directions and weights for them is let to the user, but the following mathematical conditions [Modest 2013], allow to select sets of directions which respect the symmetry of the problem by creating sets of coordinates invariant after 90 degrees rotations and which satisfy the zeroth, first and second order moments.

$$\int_{4\pi} d\Omega = 4\pi = \sum_{i=1}^{n} w_i \tag{A.2}$$

$$\int_{4\pi} \vec{\Omega} d\Omega = \vec{0} = \sum_{i=1}^{n} w_i \vec{\Omega}_i \tag{A.3}$$

$$\int_{4\pi} \vec{\Omega}\vec{\Omega} d\Omega = \frac{4\pi}{3}\vec{\delta} = \sum_{i=1}^{n} w_i \vec{\Omega}_i \vec{\Omega}_i \tag{A.4}$$

Table A.1 shows the set of equations used on the Finite Volume algorithm. In the table, ξ, η and μ represent, respectively, the direction cosines of direction Ω over each of the principal orientations $\vec{i}$, $\vec{j}$ and $\vec{k}$, as follows:

$$\vec{\Omega} = (\vec{\Omega} \cdot \vec{i})\vec{i} + (\vec{\Omega} \cdot \vec{j})\vec{j} + (\vec{\Omega} \cdot \vec{k})\vec{k} = \xi\vec{i} + \eta\vec{j} + \mu\vec{k} \tag{A.5}$$

where δ is the unit tensor.

Order of Approximation	Ordinates ξ	η	μ	Weights w
S_2 (symmetric)	0.5773503	0.5773503	0.5773503	1.5707963
S_2 (nonsymmetric)	0.5000000	0.7071068	0.5000000	1.5707963
S_4	0.2958759	0.2958759	0.9082483	0.5235987
	0.2958759	0.9082483	0.2958759	0.5235987
	0.9082483	0.2958759	0.2958759	0.5235987
S_6	0.1838670	0.1838670	0.9656013	0.1609517
	0.1838670	0.6950514	0.6950514	0.3626469
	0.1838670	0.9656013	0.1838670	0.1609517
	0.6950514	0.1838670	0.6950514	0.3626469
	0.6950514	0.6950514	0.1838670	0.3626469
	0.9656013	0.1838670	0.1838670	0.1609517
S_8	0.1422555	0.1422555	0.9795543	0.1712359
	0.1422555	0.5773503	0.8040087	0.0992284
	0.1422555	0.8040087	0.5773503	0.0992284
	0.1422555	0.9795543	0.1422555	0.1712359
	0.5773503	0.1422555	0.8040087	0.0992284
	0.5773503	0.5773503	0.5773503	0.4617179
	0.5773503	0.8040087	0.1422555	0.0992284
	0.8040087	0.1422555	0.5773503	0.0992284
	0.8040087	0.5773503	0.1422555	0.0992284
	0.9795543	0.1422555	0.1422555	0.1712359

Figure A.1: Discrete ordinates for some of the values of the S_N method [Modest 2013]

The values given in the table cover only one eight of the solid angle spectrum, as the table only shows the positive values for the cosines. To get the whole spectrum, each of the values in the table can be positive or negative, so that each of the rows contains 8 different directions.

Appendix B

Configuration CFD file

This appendix shows the configuration file that has been generated for the Huygens test-case, as an example on how a configuration file for a re-entry computation in COOLFluiD must be performed.

```
##############################################################################
#
# This COOLFluiD CFcase file tests:
#
# Finite Volume DOM algorithm, PhysicalModelDummy, EmptyIterator, hybrid mesh,
# only radiation transport (no flow) is computed, Tecplot2CFmesh converter,
# Huygens, validation case for ESA ABLARADABLA, input DLR solution
#
##############################################################################

# COOLFluiD CFcase file
# Comments begin with "#"

### Residual = 0

#CFEnv.ErrorOnUnusedConfig = true
#CFEnv.ExceptionLogLevel = 200
CFEnv.ExceptionDumps   = false
CFEnv.ExceptionOutputs = false
CFEnv.OnlyCPU0Writes = true
#CFEnv.TraceToStdOut = true

# Simulation Modules
# COOLFluiD modules to be included in the simulation
```

```
Simulator.Modules.Libs = libTecplotWriter libMutationppI libPhysicalModelDummy
    libFiniteVolume libEmptyConvergenceMethod libRadiativeTransfer
    libTecplot2CFmesh libCFmeshFileReader libCFmeshFileWriter
    libConcurrentCoupler

# relative path to working directory
Simulator.Paths.WorkingDir = plugins/RadiativeTransfer/testcases/HuygensDLR
# relative path to results directory
Simulator.Paths.ResultsDir = ./RESULTS_HUYGENS_VISCOUS

Maestro = LoopMaestro
LoopMaestro.GlobalStopCriteria = GlobalMaxNumberSteps
LoopMaestro.GlobalMaxNumberSteps.nbSteps = 1
#LoopMaestro.AppendIter = true
#LoopMaestro.RestartFromPreviousSolution = true


Simulator.SubSystems = SubSystemA SubSystem
Simulator.SubSystemTypes = OnlyMeshSubSystem StandardSubSystem

//////////////////////////////////////////////////////////////////////////////
//////////////////////////////////////////////////////////////////////////////
# SubSystemA converts from Tecplot to a CFmesh file serially (from just 1 CPU)
//////////////////////////////////////////////////////////////////////////////
//////////////////////////////////////////////////////////////////////////////

#Next lines specify the dimensions of the probem, the physical model used (for
    this case, an uncoupled system, and the equations to be considered along the
     simulation).

Simulator.SubSystemA.Default.PhysicalModelType = PhysicalModelDummy
Simulator.SubSystemA.PhysicalModelDummy.Dimensions = 3
Simulator.SubSystemA.PhysicalModelDummy.Equations = \
        rhoN2 rhoN rhoCH4 rhoCH3 rhoCH2 rhoCH rhoC2 rhoC rhoH2 rhoH rhoNH
           rhoHCN rhoCN p T Mach

# The following lines are used to convert the mesh from a Tecplot format to a
    COOLFluiD #CFmesh format

Simulator.SubSystemA.MeshCreator                                =
    CFmeshFileReader
Simulator.SubSystemA.CFmeshFileReader.Data.FileName             =
    huygens_viscous_DLR.CFmesh
```

```
Simulator.SubSystemA.CFmeshFileReader.convertFrom                =
    Tecplot2CFmesh
Simulator.SubSystemA.CFmeshFileReader.Tecplot2CFmesh.Discontinuous  = true
Simulator.SubSystemA.CFmeshFileReader.Tecplot2CFmesh.SolutionOrder  = P0
Simulator.SubSystemA.CFmeshFileReader.Tecplot2CFmesh.HasBlockFormat = false
Simulator.SubSystemA.CFmeshFileReader.Tecplot2CFmesh.SurfaceTRS = B_3 B_4 B_6
# Read the variables of the flow solution
Simulator.SubSystemA.CFmeshFileReader.Tecplot2CFmesh.ReadVariables = \
        "N2_partial_density" "N_partial_density" "CH4_partial_density" "
           CH3_partial_density" "CH2_partial_density" \
        "CH_partial_density" "C2_partial_density" "C_partial_density" "
           H2_partial_density" "H_partial_density" \
        "NH_partial_density" "HCN_partial_density" "CN_partial_density" "
           pressure" "temperature" "Mach_number"
Simulator.SubSystemA.CFmeshFileReader.Tecplot2CFmesh.NbElementTypes = 2
Simulator.SubSystemA.CFmeshFileReader.Tecplot2CFmesh.SkipSolution = false
Simulator.SubSystemA.CFmeshFileReader.Tecplot2CFmesh.Precision = 12
Simulator.SubSystemA.CFmeshFileReader.onlyConversion = true

##############################################################################
##############################################################################
# SubSystem solves radiation in parallel with each CPU loading the full mesh
##############################################################################
##############################################################################

# 8 cores for radiation
Simulator.SubSystem.Namespaces = Rad|8 RadCoupler
Simulator.SubSystem.Ranks = 0:7 0:7
# this flag ensures that coupling namespaces are filtered out during some core
    operations
Simulator.SubSystem.RadCoupler.IsForCoupling = true

####################
## Meshdata
####################
Simulator.SubSystem.Rad&8.SubSystemStatus = SubSystemStatusRad&8
Simulator.SubSystem.Rad&8.MeshData = MeshDataRad&8
Simulator.SubSystem.MeshDataRad&8.Namespaces = Rad&8
Simulator.SubSystem.MeshDataRad&8.listTRS = B_3 B_4 B_6

####################
## Physical model
####################
```

```
Simulator.SubSystem.Rad&8.PhysicalModelType = PhysicalModelDummy
Simulator.SubSystem.Rad&8.PhysicalModelName = PMRad&8
Simulator.SubSystem.PMRad&8.Dimensions = 3
Simulator.SubSystem.PMRad&8.Equations = \
        rhoN2 rhoN rhoCH4 rhoCH3 rhoCH2 rhoCH rhoC2 rhoC rhoH2 rhoH rhoNH
           rhoHCN rhoCN p T Mach


# Mutation++
# Specifies the mixture and the model used by the Mutation++ library. To check,
     but needed if the flowfield solution or any transport properties are needed
    .

Simulator.SubSystem.PMRad&8.PropertyLibrary = Mutationpp
Simulator.SubSystem.PMRad&8.Mutationpp.mixtureName = titan19
#CO25
#air11nasa9 #air11
Simulator.SubSystem.PMRad&8.Mutationpp.StateModelName = ChemNonEq1T

####################
## Output
####################
Simulator.SubSystem.OutputFormat      = Null~7 Tecplot
Simulator.SubSystem.OutputFormatNames = Null@7 Tecplot7
Simulator.SubSystem.Tecplot7.Namespace = Rad7
Simulator.SubSystem.Tecplot7.FileName  = huygens_viscous_DLR_rad7.plt
Simulator.SubSystem.Tecplot7.Data.SurfaceTRS = B_3 B_4 B_6
Simulator.SubSystem.Tecplot7.SaveRate = 100
Simulator.SubSystem.Tecplot7.AppendIter = false
Simulator.SubSystem.Tecplot7.Data.DataHandleOutput.CCSocketNames = CellID divq
    qx qy qz
Simulator.SubSystem.Tecplot7.Data.DataHandleOutput.CCVariableNames = CellID
    divq qx qy qz
Simulator.SubSystem.Tecplot7.Data.DataHandleOutput.CCBlockSize = 1 1 1 1 1
Simulator.SubSystem.Tecplot7.WriteSol = ParWriteSolutionBlock
Simulator.SubSystem.Tecplot7.Data.CollaboratorNames = SMRad7
Simulator.SubSystem.Null&7.Namespace = Rad&7
Simulator.SubSystem.Null&7.Data.CollaboratorNames = SMRad&7

#Simulator.SubSystem.OutputFormat      = Tecplot~8
#Simulator.SubSystem.OutputFormatNames = Tecplot@8
#Simulator.SubSystem.Tecplot&8.Namespace = Rad&8
#Simulator.SubSystem.Tecplot&8.FileName  = huygens_viscous_DLR_rad&8.plt
```

```
#Simulator.SubSystem.Tecplot&8.Data.SurfaceTRS = B_3 B_4 B_6
#Simulator.SubSystem.Tecplot&8.SaveRate = 100
#Simulator.SubSystem.Tecplot&8.AppendIter = false
#Simulator.SubSystem.Tecplot&8.Data.DataHandleOutput.CCSocketNames = CellID
   divq qx qy qz TempProfile
#Simulator.SubSystem.Tecplot&8.Data.DataHandleOutput.CCVariableNames = CellID
   divq qx qy qz TempProfile
#Simulator.SubSystem.Tecplot&8.Data.DataHandleOutput.CCBlockSize = 1 1 1 1 1 1
#Simulator.SubSystem.Tecplot&8.WriteSol = ParWriteSolutionBlock
#Simulator.SubSystem.Tecplot&8.Data.CollaboratorNames = SMRad&8
#Simulator.SubSystem.Tecplot&8.Data.WithEquations = false

####################
## Stop condition
####################
Simulator.SubSystem.StopCondition          = MaxNumberSteps
Simulator.SubSystem.MaxNumberSteps.nbSteps = 1~8 1~8

#Simulator.SubSystem.StopCondition       = Norm
#Simulator.SubSystem.Norm.valueNorm      = -7.0

####################
## Input
####################
Simulator.SubSystem.MeshCreator      = CFmeshFileReader~8
Simulator.SubSystem.MeshCreatorNames = CFmeshFileReader@8

Simulator.SubSystem.CFmeshFileReader&8.Namespace = Rad&8
Simulator.SubSystem.CFmeshFileReader&8.Data.FileName = huygens_viscous_DLR.
   CFmesh
Simulator.SubSystem.CFmeshFileReader&8.Data.ScalingFactor = 1.
Simulator.SubSystem.CFmeshFileReader&8.ParReadCFmesh.ParCFmeshFileReader.
   ParMetis.NCommonNodes = 3
Simulator.SubSystem.CFmeshFileReader&8.Data.CollaboratorNames = SMRad&8

####################
## Linear system
####################
Simulator.SubSystem.LinearSystemSolver  = Null~8
Simulator.SubSystem.LSSNames            = LSSRad@8
Simulator.SubSystem.LSSRad&8.Namespace = Rad&8

####################
```

```
## Time integrator
####################
Simulator.SubSystem.ConvergenceMethod = EmptyIterator~8
Simulator.SubSystem.ConvergenceMethodNames = IteratorRad@8
Simulator.SubSystem.IteratorRad&8.Namespace = Rad&8

####################
## Space Method
####################
Simulator.SubSystem.SpaceMethod      = CellCenterFVM~8
Simulator.SubSystem.SpaceMethodNames = SMRad@8
Simulator.SubSystem.SMRad&8.Namespace = Rad&8
Simulator.SubSystem.SMRad&8.Data.CollaboratorNames = LSSRad&8 IteratorRad&8
Simulator.SubSystem.SMRad&8.ComputeRHS = Null
Simulator.SubSystem.SMRad&8.Restart = true

##############################################################################

# Data Processing
# Parameters that create the options for the Finite Volume Solver, including
    every option explained in the thesis: Exponential or non-exponential methods
    , number of directions...
Simulator.SubSystem.DataPostProcessing = DataProcessing~8
Simulator.SubSystem.DataPostProcessingNames = ProcessingRad@8
Simulator.SubSystem.ProcessingRad&8.Namespace = Rad&8
Simulator.SubSystem.ProcessingRad&8.Data.CollaboratorNames = SMRad&8
    IteratorRad&8 LSSRad&8
Simulator.SubSystem.ProcessingRad&8.Comds = RadiativeTransferFVDOM
Simulator.SubSystem.ProcessingRad&8.Names = Radiation
Simulator.SubSystem.ProcessingRad&8.Radiation.nDirs =  48
Simulator.SubSystem.ProcessingRad&8.Radiation.UseExponentialMethod = true
#Simulator.SubSystem.ProcessingRad&8.Radiation.DirName = ./
Simulator.SubSystem.ProcessingRad&8.Radiation.BinTabName = air-100Bands.dat #
    air-100Bins.dat
Simulator.SubSystem.ProcessingRad&8.Radiation.OutTabName = air-100Bands.out #
    air-100Bins.out
#Simulator.SubSystem.ProcessingRad&8.Radiation.ConstantP = 1013250
Simulator.SubSystem.ProcessingRad&8.Radiation.PID = 13
Simulator.SubSystem.ProcessingRad&8.Radiation.TID = 14
Simulator.SubSystem.ProcessingRad&8.ProcessRate = 1
#Simulator.SubSystem.ProcessingRad&8.RunAtSetup = true
Simulator.SubSystem.ProcessingRad&8.Radiation.OldAlgorithm = false
```

```
# here we need to find a way to write expression
Simulator.SubSystem.ProcessingRad&8.Radiation.NbThreads = 8
Simulator.SubSystem.ProcessingRad&8.Radiation.ThreadID  = &8
# if the following is "false" with 8 directions and 100 bins you have:
# a matrix nbDirections*nbBins => with 8 CPUs, each CPU gets 1 direction and
    100 bins
# if the following is "true" with 8 directions and 100 bins you have:
# a matrix nbBins*nbDirections => with 100 CPUs, each CPU gets 1 bin and 8
    directions
Simulator.SubSystem.ProcessingRad&8.Radiation.LoopOverBins = false
Simulator.SubSystem.ProcessingRad&8.Radiation.BinningPARADE = true

# PARADE-related settings
# Configuration options for the PARADE radiator, mainly the wavelength interval
    , the type of radiator system used, the number of bins or bands and the
    number of discretization points.

Simulator.SubSystem.ProcessingRad&8.Radiation.RadiationPhysicsHandler.
    NumberLoops = 1
Simulator.SubSystem.ProcessingRad&8.Radiation.RadiationPhysicsHandler.TempID =
    14
Simulator.SubSystem.ProcessingRad&8.Radiation.RadiationPhysicsHandler.
    WavelengthMax = 150000
Simulator.SubSystem.ProcessingRad&8.Radiation.RadiationPhysicsHandler.
    WavelengthMin = 3000
Simulator.SubSystem.ProcessingRad&8.Radiation.RadiationPhysicsHandler.
    RadiationPhysicsNames = aa
Simulator.SubSystem.ProcessingRad&8.Radiation.RadiationPhysicsHandler.aa.
    ApplyTRS   = InnerCells
Simulator.SubSystem.ProcessingRad&8.Radiation.RadiationPhysicsHandler.aa.
    TypeTRS    = Medium
Simulator.SubSystem.ProcessingRad&8.Radiation.RadiationPhysicsHandler.aa.
    Radiator   = ParadeRadiator
# this is fundamental for letting PARADE rn in parallel
Simulator.SubSystem.ProcessingRad&8.Radiation.RadiationPhysicsHandler.aa.
    ParadeRadiator.Namespace = RadCoupler
Simulator.SubSystem.ProcessingRad&8.Radiation.RadiationPhysicsHandler.aa.
    ParadeRadiator.LibraryPath = \
/data/jmartinez/parade_mycopy
#/software/alternate/coolfluid/cf2/2015.11/parade-3.2.1_INTEL
#       /software/alternate/coolfluid/cf2/2015.11/parade-3.2.1_INTEL
#       /Users/lani/PARADEv3.2.1/parade-3.2.1
#       /software/alternate/coolfluid/cf2/2015.11/parade-3.2.1_INTEL
```

```
Simulator.SubSystem.ProcessingRad&8.Radiation.RadiationPhysicsHandler.aa.
    ParadeRadiator.LocalDirName = ParadeData
Simulator.SubSystem.ProcessingRad&8.Radiation.RadiationPhysicsHandler.aa.
    ParadeRadiator.nbPoints = 1000
Simulator.SubSystem.ProcessingRad&8.Radiation.RadiationPhysicsHandler.aa.
    ParadeRadiator.Tmin = 200
Simulator.SubSystem.ProcessingRad&8.Radiation.RadiationPhysicsHandler.aa.
    ParadeRadiator.ReuseProperties = true
Simulator.SubSystem.ProcessingRad&8.Radiation.RadiationPhysicsHandler.aa.
    ParadeRadiator.MolecularSpecies = 1 0 1 1 1 1 1 0 1 0 1 1 1
#Simulator.SubSystem.ProcessingRad&8.Radiation.RadiationPhysicsHandler.aa.
    ParadeRadiator.WriteHSNB = false
#Check that this number of bins is equal to the number stated in the Finite
    Volume configuration options
Simulator.SubSystem.ProcessingRad&8.Radiation.RadiationPhysicsHandler.aa.
    ParadeRadiator.Binning = true
Simulator.SubSystem.ProcessingRad&8.Radiation.RadiationPhysicsHandler.aa.
    ParadeRadiator.nbBins = 100
Simulator.SubSystem.ProcessingRad&8.Radiation.RadiationPhysicsHandler.aa.
    ParadeRadiator.Banding = false
Simulator.SubSystem.ProcessingRad&8.Radiation.RadiationPhysicsHandler.aa.
    ParadeRadiator.nbBands = 1


Simulator.SubSystem.ProcessingRad&8.Radiation.RadiationPhysicsHandler.b1.
    ApplyTRS   = B_3
Simulator.SubSystem.ProcessingRad&8.Radiation.RadiationPhysicsHandler.b1.
    TypeTRS    = Wall
Simulator.SubSystem.ProcessingRad&8.Radiation.RadiationPhysicsHandler.b1.
    Radiator = GreyWallRadiator
Simulator.SubSystem.ProcessingRad&8.Radiation.RadiationPhysicsHandler.b1.
    GreyWallRadiator.ElemAbsCoeff = 0.6
Simulator.SubSystem.ProcessingRad&8.Radiation.RadiationPhysicsHandler.b1.
    GreyWallRadiator.ElemEmsCoeff = 0.

Simulator.SubSystem.ProcessingRad&8.Radiation.RadiationPhysicsHandler.b2.
    ApplyTRS   = B_4
Simulator.SubSystem.ProcessingRad&8.Radiation.RadiationPhysicsHandler.b2.
    TypeTRS    = Boundary


Simulator.SubSystem.ProcessingRad&8.Radiation.RadiationPhysicsHandler.b3.
    ApplyTRS   = B_6
```

```
Simulator.SubSystem.ProcessingRad&8.Radiation.RadiationPhysicsHandler.b3.
    TypeTRS     = Boundary

# fictitious coupling model
Simulator.SubSystem.RadCoupler.SubSystemStatus = RadCouplerSubSystemStatus
Simulator.SubSystem.RadCoupler.MeshData = RadCouplerMeshData
Simulator.SubSystem.RadCouplerMeshData.Namespaces = RadCoupler
#Simulator.SubSystem.RadCouplerMeshData.listTRS =
Simulator.SubSystem.RadCoupler.PhysicalModelType = CouplingModelDummy
Simulator.SubSystem.RadCoupler.PhysicalModelName = RadCouplerPM
Simulator.SubSystem.RadCouplerPM.Dimensions = 3
Simulator.SubSystem.RadCouplerPM.Equations = divq qx qy qz
# the following will be used by CouplingModelDummySendToRecv to transfer states
Simulator.SubSystem.RadCouplerPM.SendIDs = 0
Simulator.SubSystem.RadCouplerPM.RecvIDs = 0

Simulator.SubSystem.CouplerMethod = ConcurrentCoupler
Simulator.SubSystem.ConcurrentCoupler.CommandGroups = RadInteraction
Simulator.SubSystem.ConcurrentCoupler.Namespace = RadCoupler
Simulator.SubSystem.ConcurrentCoupler.CoupledNameSpaces = Rad@8
Simulator.SubSystem.ConcurrentCoupler.CoupledSubSystems = SubSystem~8
Simulator.SubSystem.ConcurrentCoupler.TransferRates = 1~8
# hose two oprions are fundamental for this case to run properly
Simulator.SubSystem.ConcurrentCoupler.SkipFirstCouplingIter = false #true
Simulator.SubSystem.ConcurrentCoupler.ImposeSynchronization = true
# need an interface write coms that uses MPI_Reduce of MPI_Allreduce for all
    Rad*_divq
Simulator.SubSystem.ConcurrentCoupler.InterfacesWriteComs = StdConcurrentReduce
Simulator.SubSystem.ConcurrentCoupler.InterfacesWriteNames = ReduceRad
# first globally reduce all qrad contributions from all Rad* namespaces
Simulator.SubSystem.ConcurrentCoupler.ReduceRad.SocketsSendRecv = Rad_divq
    Rad_qx Rad_qy Rad_qz
Simulator.SubSystem.ConcurrentCoupler.ReduceRad.SocketsConnType = State State
    State State
Simulator.SubSystem.ConcurrentCoupler.ReduceRad.Operation = SUM SUM SUM SUM
```

Appendix C

Radiative processes in gaseous media

Although the objective of this thesis is not to provide an extense cover of all the hypersonic phenomena which have an influence on the behavior of the spacecraft in reentries, a brief description of the processes which generated the radiative transfer must be provided to acquire an overview of the problem. These processes can be divided into three categories:

C.0.1 Bound-bound processes

Bound-bound processes are generated by a radiative transition between two bound energy levels of a species. They appear under three mechanisms, namely, absorption, emission and stimulated emission, which are described by the following reaction mechanisms:

- Absorption

$$A(l) + hc\sigma_{ul} \rightarrow A(u)$$

- Spontaneous emission

$$A(u) \rightarrow A(l) + hc\sigma_{ul}$$

- Stimulated emission

$$A(u) + hc\sigma_{ul} \rightarrow A(l) + 2hc\sigma_{ul}$$

where σ_{ul} is the wavenumber of the absorbed or emitted photon. These three mechanisms are activated due to the emission and absorption of photons. The difference betweenthe energy of lthe levels is described by the photon energy $hc\sigma$, so that:

$$E_u - E_l = hc\sigma \tag{C.1}$$

Bound bound transitions result in discrete spectral lines, which correspond to the emission and absorption of these specific photon energies. These lines are centered around the wavelength of the transition energy.

C.0.2 Bound-free mechanisms

If we consider now transitions between bounded and unbounded states, we have the group of the bound free processes, in which we encounter photoionization, photodissociation, dissociative photoionization and photodetachment.

- Photoionization

$$A + hc\sigma \rightarrow A^+ + e^-$$

- Photodissociation

$$AB + hc\sigma \rightarrow A + B$$

- Dissociative photoionization

$$AB + hc\sigma \rightarrow A + B^+ + e^-$$

- Photodetachment processes

$$A^- + hc\sigma \rightarrow A + e^-$$

C.0.3 Free-free mechanisms

Finally, the collisions between electrons and other particles like ions, atoms or molecules, which slows in turn these electrons, is called free-free emission or Bremsstrahlung effect. This mechanism, which is in fact continuous because of the nature of the translational energy of these free electrons, can be described by the following expression:

$$A + e^- = A + e^- + hc\sigma \tag{C.2}$$

More information about these radiative transitions can be found in [Soufiani 2008].

Bibliography

[Alvarez 2016] A. Alvarez, N. N. Mansour, A. K. Lonkar, A. Lani et A. Wray. *Formulation of the MFD Equations*. NASA Ames internal notes, 2016.

[Bottin 2000] B. Bottin, O. Chazot, M. Carbonaro, V. Van Der Haegen et S. Paris. *The VKI Plasmatron Characteristics and Performance*. von Karman Institute for Fluid Dynamics, Internal Release, 2000.

[Caliot 2010] C. Caliot. *Numerical Methods in Radiative Transfer*. PROMES-CNRS, 2010.

[Göbel 2012] F. Göbel, J. B. Vos et C. Mundt. *CFD Simulation of the FIRE II Flight Experiment*. 42nd AIAA Fluid Dynamics Conference and Exhibit, AIAA 2012-3350, 2012.

[Johnston 2008] C. O. Johnston, B. Hollis et K. Sutton. *Nonequilibrium Stagnation-Line Radiative for Fire II*. Journal of Spacecraft and Rockets, vol. 45, no. 6, pages 1185–1195, 2008.

[Karl 2011] S. Karl. *Performance of Sensitivity Analysis for Fire and Huygens Entry*. Validation of Aerothermochemistry Models for Re-entry Applications, Technical Note 8.2, WP6200, 2011.

[Karl 2013] S. Karl, D. Potter, M. Lambert et K. Hannemann. *Computational Analysis of Radiative Heat Loading on Hypervelocity Reentry Vehicles*. Journal of Spacecraft and Rockets, vol. 52, no. 1, pages 63–75, 2013.

[Lani 2013] A. Lani, N. Villedieu, K. Bensassi et M. Sarp Yalim. *COOLFluiD: an open computational platform for multi-physics simulation*. 21st AIAA Computational Fluid Dynamics Conference, AIAA 2013-2589, 2013.

[Lopez 2013] B. Lopez, M. Y. Perrin, P. Rivière et A. Soufiani. *Coupled Nonequilibrium Flowfield-Radiative Transfer Calculation Behind a Shock Wave*. Journal of Thermophysics and Heat Transfer, vol. 27, no. 3, pages 404–413, 2013.

[Mazoué 2005] F. Mazoué et L. Marrafa. *Flow-field/Radiation Coupling Analyisis for Huygens Probe Entry into Titan atmosphere*. 38th AIAA Thermophysics Conference, 2005.

[Meurisse 2016] J. Meurisse et N. Mansour. *Technical notes.* Advanced Supercomputing Division, NASA Ames Research Center, Arc Jet Facilities, 2016.

[Modest 2013] M. F. Modest. Radiative heat transfer. Academic Press, 2013.

[Potter 2013] D. Potter, S. Karl, M. Lambert et K. Hannemann. *Computation of radiative and convective contributions to Viking afterbody heating.* 44th AIAA Thermophysics Conference, 2013.

[Richards] B. E. Richards et K. R. Enkenhus. *Hypersonic Testing in the VKI Longshot Free-Piston Tunnel.* AIAA Journal, vol. 8, no. 6, pages 1020–1025.

[Santos 2016] P. D. Santos et A. Lani. *An object-oriented implementation of a parallel Monte Carlo code for radiation transport.* Computer Physics Communications, vol. 202, page 233–261, 2016.

[Scoggins] J. B. Scoggins, L. Soucasse, P. Rivière, A. Soufiani et T. Magin. *Coupled Flow, Radiation, and Ablation Simulations of Atmospheric Entry Vehicles using the Hybrid Statistical Narrow Band Model.* 45th AIAA Thermophysics Conference, AIAA-2015-3112.

[Scoggins 2013] J. B. Scoggins, T. Magin, A. Wray et Mansour N. N. *Multi-Group Reductions of LTE Air Plasma Radiative Transfer in Cylindrical Geometries.* 44th AIAA Thermophysics Conference, 2013.

[Scoggins 2014] J. B. Scoggins et T. E. Magin. *Development of Mutation++: Multicomponent Thermodynamic and Transport Properties for Ionized Plasmas written in C++.* 11th AIAA/ASME Joint Thermophysics and Heat Transfer Conference, 10.2514/6.2014-2966, 2014.

[Smith 2010] A. J. Smith, J. Beck, M. Fertig, H. Liebhart et L. Marrafa. Plasma radiation database parade v2.3d, final report issue 5. Fluid Gravity Engineering LTD, 2010.

[Soufiani 2008] A. Soufiani, P. Rivière et M. Y. Perrin. *Radiation Database for Earth and Mars Entry, ADA569303.* 2008.

[Vincenti 1986] W. G. Vincenti et C. H. Kruger. Physical gas dynamics. Robert E. Krieger Publishing Co., Inc, 1986.

[Vogler 2004] A. Vogler, J. Bruls et M. Schussler. *Approximations for non-grey radiative transfer in numerical simulations of the solar photosphere.* Astronomy Astrophysics, pages 741 – 754, 2004.

[Wray 2006] A. A. Wray, J. F. Ripoll et D. Prabhu. *Investigation of the opacity binning approach for solving the shock-generated radiation of the Apollo AS-501 re-entry.* Proceedings of the Summer Program, NASA, 2006.

[Wray 2012] A. Wray. *Improved Finite Volume Method for Radiative Hydrodynamics*. Seventh International Conference on Computational Fluid Dynamics (ICCFD7), 2012.

[Wright 2003] M. Wright, M. Loomis et P. Papadopoulos. *Aerothermal Analysis of the Project Fire II Afterbody Flow*. Journal of Thermophysics and Heat Transfer, vol. 17, no. 2, pages 240 – 249, 2003.

Abstract The work over this report has intended to provide a broad vision of how the radiative processes impact the heat fluxes that appear on a reentry process, and to describe the implemented ways to assess its computation.

von Karman Institute for Fluid Dynamics
72, Chaussée de Waterloo
1640 Rhode-Saint-Genèse
Belgium